The Astrophysical Journal, 979:229 (20pp), 2025 February 1 https://doi.org/10.3847/1538-4357/ada357

SCUBADive. I. JWST+ALMA Analysis of 289 Submillimeter Galaxies in COSMOS-web

Jed McKinney[1,37], Caitlin M. Casey[1], Arianna S. Long[1,37], Olivia R. Cooper[1,38], Sinclaire M. Manning[2,37], Maximilien Franco[1], Hollis Akins[1,38], Erini Lambrides[3,39], Elaine Gammon[4,40], Camila Silva[1,5], Fabrizio Gentile[6,7], Jorge A. Zavala[8], Aristeidis Amvrosiadis[9,10], Irham Andika[11,12], Malte Brinch[13,14], Jaclyn B. Champagne[15], Nima Chartab[16], Nicole E. Drakos[17], Andreas L. Faisst[16], Seiji Fujimoto[1,37], Steven Gillman[13,14], Ghassem Gozaliasl[18,19], Thomas R. Greve[13,14,20], Santosh Harish[21], Christopher C. Hayward[22], Michaela Hirschmann[23,24], Olivier Ilbert[25], Boris S. Kalita[26,27,28,41], Jeyhan S. Kartaltepe[21], Anton M. Koekemoer[29], Vasily Kokorev[1], Daizhong Liu[30], Georgios Magdis[13,14,31], Henry Joy McCracken[32], Jason Rhodes[33], Brant E. Robertson[34], Margherita Talia[6,7], Francesco Valentino[13,35], and Aswin P. Vijayan[36]

[1] Department of Astronomy, The University of Texas at Austin, Austin, TX 78712, USA
[2] Department of Astronomy, University of Massachusetts Amherst, 710 N. Pleasant Street, Amherst, MA 01003, USA
[3] NASA-Goddard Space Flight Center, Code 662, Greenbelt, MD 20771, USA
[4] Department of Physics & Astronomy, University of Georgia, Sanford Drive, Athens, GA 30602, USA
[5] Department of Astronomy and Astrophysics, The University of Chicago, Chicago, IL 60637, USA
[6] University of Bologna—Department of Physics and Astronomy "Augusto Righi" (DIFA), Via Gobetti 93/2, I-40129 Bologna, Italy
[7] INAF—Osservatorio di Astrofisica e Scienza dello Spazio, Via Gobetti 93/3, I-40129, Bologna, Italy
[8] National Astronomical Observatory of Japan, 2-21-1 Osawa, Mitaka, Tokyo 181-8588, Japan
[9] Centre for Extragalactic Astronomy, Durham University, South Road, Durham, DH1 3LE, UK
[10] Institute for Computational Cosmology, Durham University, South Road, Durham, DH1 3LE, UK
[11] TUM School of Natural Sciences, Department of Physics,Technical University of Munich, James-Franck-Str. 1, D-85748 Garching, Germany
[12] Max-Planck-Institut fur Astrophysik, Karl-Schwarzschild-Str. 1, D-85748 Garching, Germany
[13] Cosmic Dawn Center (DAWN), Copenhagen, Denmark
[14] DTU-Space, Technical University of Denmark, Elektrovej 327, 2800, Kgs. Lyngby, Denmark
[15] Steward Observatory, University of Arizona, 933 N. Cherry Ave., Tucson, AZ 85721, USA
[16] Caltech/IPAC, 1200 E. California Blvd., Pasadena, CA 91125, USA
[17] Department of Physics and Astronomy, University of Hawaii, Hilo, 200 W. Kawili St., Hilo, HI 96720, USA
[18] Department of Computer Science, Aalto University, P.O. Box 15400, FI-00076 Espoo, Finland
[19] Department of Physics, University of Helsinki, P.O. Box 64, FI-00014 Helsinki, Finland
[20] Department of Physics and Astronomy, University College London, Gower Street, London, WC1E 6BT, UK
[21] Laboratory for Multiwavelength Astrophysics, School of Physics and Astronomy, Rochester Institute of Technology, 84 Lomb Memorial Drive, Rochester, NY 14623, USA
[22] Center for Computational Astrophysics, Flatiron Institute, 162 Fifth Avenue, New York, NY 10010, USA
[23] Institute of Physics, GalSpec, Ecole Polytechnique Federale de Lausanne, Observatoire de Sauverny, Chemin Pegasi 51, 1290 Versoix, Switzerland
[24] INAF, Astronomical Observatory of Trieste, Via Tiepolo 11, 34131 Trieste, Italy
[25] Aix Marseille Univ, CNRS, CNES, LAM, Marseille, France
[26] Kavli Institute for the Physics and Mathematics of the Universe, The University of Tokyo, Kashiwa, 277-8583, Japan
[27] Kavli Institute for Astronomy and Astrophysics, Peking University, Beijing 100871, People's Republic of China
[28] Center for Data-Driven Discovery, Kavli IPMU (WPI), UTIAS, The University of Tokyo, Kashiwa, Chiba 277-8583, Japan
[29] Space Telescope Science Institute, 3700 San Martin Dr., Baltimore, MD 21218, USA
[30] Purple Mountain Observatory, Chinese Academy of Sciences, 10 Yuanhua Road, Nanjing 210023, People's Republic of China
[31] Niels Bohr Institute, University of Copenhagen, Jagtvej 128, DK-2200, Copenhagen, Denmark
[32] Institut d'Astrophysique de Paris, UMR 7095, CNRS, and Sorbonne Université, 98 bis boulevard Arago, F-75014 Paris, France
[33] Jet Propulsion Laboratory, California Institute of Technology, 4800 Oak Grove Drive, Pasadena, CA 91001, USA
[34] Department of Astronomy and Astrophysics, University of California, Santa Cruz, 1156 High Street, Santa Cruz, CA 95064, USA
[35] European Southern Observatory, Karl-Schwarzschild-Str. 2, D-85748, Garching bei Munchen, Germany
[36] Astronomy Centre, University of Sussex, Falmer, Brighton, BN1 9QH, UK
Received 2024 August 15; revised 2024 November 15; accepted 2024 December 9; published 2025 January 29

Abstract

JWST has enabled detecting and spatially resolving the heavily dust-attenuated stellar populations of submillimeter galaxies, revealing detail that was previously inaccessible. In this work, we construct a sample of 289 submillimeter galaxies with joint Atacama Large Millimeter/submillimeter Array (ALMA) and JWST constraints in the COSMOS field. Sources are originally selected using the SCUBA-2 instrument and have archival ALMA observations from various programs. Their JWST NIRCam imaging is from COSMOS-Web and PRIMER. We extract multiwavelength photometry in a manner that leverages the unprecedented near-infrared (NIR) spatial

[37] NASA Hubble Fellow.
[38] NSF Graduate Research Fellow.
[39] NPP Fellow.
[40] Goldwater Scholar.
[41] Kavli Astrophysics Fellow.

resolution of JWST, and we fit the data with spectral energy distribution models to derive photometric redshifts, stellar masses, star formation rates, and optical attenuation. The sample has an average $\langle z\rangle = 2.6^{+1.0}_{-0.8}$, $\langle A_V\rangle = 2.5^{+1.5}_{-1.0}$, $\langle \mathrm{SFR}\rangle = 300^{+400}_{-200}\,M_\odot\,\mathrm{yr}^{-1}$, and $\langle \log(M_*/M_\odot)\rangle = 11.1^{+0.3}_{-0.5}$. There are 81 (30%) galaxies that have no previous optical/NIR detections, including 75% of the $z > 4$ subsample ($n = 28$). The faintest observed NIR sources have the highest redshifts and largest $A_V = 4 \pm 1$. In a preliminary morphology analysis we find that ~10% of the members of our sample exhibit spiral arms and 5% host stellar bars, with one candidate bar found at $z > 3$. Finally, we find that the clustering of JWST sources within 10″ of a submillimeter galaxy is a factor of 2 greater than what is expected based on either random clustering or the distribution of sources around any red galaxy irrespective of a submillimeter detection.

Unified Astronomy Thesaurus concepts: Galaxy evolution (594); Observational astronomy (1145); High-redshift galaxies (734); Submillimeter astronomy (1647)

Materials only available in the online version of record: figure set, machine-readable tables

1. Introduction

Extragalactic sources selected from deep and wide submillimeter fields capture galaxies in an evolutionary stage of rapid mass assembly. The aptly named "submillimeter galaxies" (SMGs; $S_{850\,\mu\mathrm{m}} \gtrsim 1$ mJy) are very luminous in the infrared (IR) with ($L_{\mathrm{IR}}/L_\odot > 10^{12}$), large stellar masses ($M_*/M_\odot \sim 10^{11}$), and typical redshifts of $z \sim 2-3$ (see, e.g., C. M. Casey et al. 2014a; J. A. Hodge & E. da Cunha 2020, for a review, and the initial discovery papers of I. Smail et al. 1997; A. J. Barger et al. 1998; D. H. Hughes et al. 1998; S. Eales et al. 1999). SMGs can form up to $100-1000\,M_\odot$ worth of new stars each year and are responsible for most of the volume-averaged star formation over the past 10 billion years (i.e., from $0 < z < 3$; E. J. Murphy et al. 2011; P. Madau & M. Dickinson 2014; J. A. Zavala et al. 2021). It is the energy from this vigorous star formation, and in some cases accreting supermassive black holes (J. McKinney et al. 2021), that heats significant reservoirs of cold dust and drives bright submillimeter emission (D. B. Sanders & I. F. Mirabel 1996). This dust simultaneously attenuates rest-frame UV/optical light, leading to typical $A_V \sim 1-5$ in SMGs (E. da Cunha et al. 2015; U. Dudzevičiūtė et al. 2020). That, combined with $\langle z\rangle = 2.5$ (E. da Cunha et al. 2015; U. Dudzevičiūtė et al. 2020), causes SMGs to be very faint in the rest-frame UV/optical. As a result, SMGs have been historically difficult to detect with ground- and space-based facilities operating in the optical/near-infrared (NIR) regime. This is especially true for SMGs at $z > 3$, which has led to a panoply of monikers like "optically faint radio galaxies," "optically dark," "NIR-dark," and "HST-dark," all used to describe such dust-obscured sources that elude detection by the most sensitive optical/NIR telescopes (e.g., S. C. Chapman et al. 2004; C. M. Casey et al. 2009; J. M. Simpson et al. 2014; T. Wang et al. 2016b; M. Franco et al. 2018; C. C. Williams et al. 2019; I. Smail et al. 2021; S. M. Manning et al. 2022; V. Kokorev et al. 2023; J. McKinney et al. 2023b; S. H. Price et al. 2023).

Thanks to JWST, the direct stellar light from SMGs is readily detectable with the NIRCam long-wavelength (LW) filters ($2.4-5\,\mu$m) up to $z \sim 6$ and $A_V \sim 6$ (C. Cheng et al. 2022; C.-C. Chen et al. 2022a; S. Gillman et al. 2023; J. McKinney et al. 2023b; W. Rujopakarn et al. 2023; Y. Wu et al. 2023; J. A. Zavala et al. 2023). This enables more robust photometric redshifts (C. M. Casey et al. 2023a), especially so for the subset of sources with no prior optical/near-IR counterpart. The inclusion of JWST bands can also dramatically impact derived stellar masses (J. McKinney et al. 2023b), thus yielding more precise constraints on the mass assembly in the Universe's most prolific star factories.

Furthermore, the angular resolution achieved by JWST enables detailed stellar morphology measurements in the SMGs, a historically impossible task given their marginal detections in, e.g., the Hubble Space Telescope (HST) Advanced Camera for Surveys (ACS)/WFC3. Recently, S. Gillman et al. (2023) studied a sample of SMGs matched to optical counterparts based on their NIRCam colors, recovering the standard SMG redshift posterior and finding compact and clumpy stellar morphologies. A. Le Bail et al. (2024) find similarly clumpy NIRCam morphologies and identify subregions of quiescence within $z \sim 2$ galaxies still undergoing active star formation. J. A. Hodge et al. (2024) report a strong correlation between the dust continuum and reddening of NIRCam colors on kiloparsec scales in 13 SMGs favoring dust obscuration as the primary source of their red rest-frame optical colors. J. McKinney et al. (2023b) use ALMA and JWST to identify an SMG at $z \sim 6$, adding to the growing sample of $z > 5$ SMGs that is coming into focus (C. C. Williams et al. 2019; Z. Chen et al. 2021). Thus, JWST is providing a new and powerful perspective on canonical $z \sim 1-3$ SMGs while also revealing stellar light in the most distant SMGs for the first time. This is profoundly changing our understanding of their physical nature, as, for example, it is difficult to test for morphological signatures of mergers without being able to detect, let alone resolve, the stellar light.

These recent works stand atop decades of thorough analysis of SMGs investigating their nature and distribution across cosmic time and environment. Indeed, multiwavelength follow-up of SMGs has been an active field, using first radio interferometers like the Very Large Array (VLA) to identify optical counterparts (A. J. Barger et al. 2000) and then later the Atacama Large Millimeter/submillimeter Array (ALMA) at submillimeter wavelengths (J. A. Hodge et al. 2013; A. Karim et al. 2013). Near- and mid-infrared follow-up campaigns have also been critical for establishing the physical nature of SMGs (A. M. Swinbank et al. 2004, 2010; S. C. Chapman et al. 2005; L. J. Hainline et al. 2009, 2011). In recent years samples have grown beyond the <100 sources typical of early pioneering studies to more than 1000 SMGs with counterparts across the multiwavelength spectrum (D. Brisbin et al. 2017; U. Dudzevičiūtė et al. 2020; J. M. Simpson et al. 2020).

In this paper, we make a statistical effort to match a large sample of SMGs identified with the SCUBA-2 submillimeter instrument to their JWST counterparts. We analyze sources in the COSMOS field (P. Capak et al. 2007; D. B. Sanders et al. 2007; N. Scoville et al. 2007) using data from the largest contiguous JWST mosaic, COSMOS-Web (C. M. Casey et al. 2023a). We use archival ALMA data to resolve the low-

resolution SCUBA-2 data on subarcsecond scales in order to identify the optical counterparts for SMGs. By construction, every source in our sample has both JWST and ALMA detections. This is the first paper in a series and precedes a thorough analysis of the JWST morphologies of SMGs, their spatially resolved stellar properties, and the subset at the highest redshifts (S. M. Manning et al. 2025, in preparation). In this work we describe our sample and comment on properties of the population as a whole.

This paper is structured as follows. In Section 2 we review the multiwavelength data sets incorporated into our work. In Section 3 we outline our sample selection criterion. Section 4 describes our reduction of archival ALMA data sets. Section 5 describes the manner in which we measure photometry for our sample across the electromagnetic spectrum. We describe our modeling of the galaxy-integrated spectral energy distributions (SEDs) in Section 6 and present the corresponding results in Section 7. Finally, we discuss the implications of our findings in Section 8. Throughout this work we assume a ΛCDM cosmology with $H_0 = 70\,\mathrm{km\,s^{-1}\,Mpc^{-1}}$, $\Omega_m = 0.3$, $\Omega_\Lambda = 0.7$, and a Chabrier initial mass function (IMF; G. Chabrier 2003). We report AB magnitudes (J. B. Oke 1974).

2. Data

Our work focuses on sources in the COSMOS extragalactic field, which hosts an extensive collection of multiwavelength data. Most relevant to this work is the JWST Cycle 1 GO program COSMOS-Web, a 0.54 deg^2 survey using NIRCam and MIRI (PID no. 1727, PIs Kartaltepe & Casey; C. M. Casey et al. 2023a) centered in the middle of the 2 deg^2 field. The NIRCam filters include two short-wavelength (SW) filters, F115W and F150W, and two LW filters, F277W and F444W. The 5σ depths in these filters range between ∼27 and 28 mag and are accompanied by a 0.19 deg^2 noncontiguous MIRI/F770W map with $5\sigma \sim 25.8$ mag (M. Franco et al. 2025, in preparation; S. Harish et al. 2025, in preparation; C. M. Casey et al. 2023a). We use the extensive compilation of rest-frame optical and NIR maps from COSMOS2020 (J. R. Weaver et al. 2022) including HST/ACS imaging from A. M. Koekemoer et al. (2007) and Spitzer/IRAC imaging from S-COSMOS (D. B. Sanders et al. 2007; Euclid Collaboration et al. 2022).

Our submillimeter sources are selected from the James Clerk Maxwell Telescope SCUBA-2 map of the COSMOS field (S2COSMOS; J. M. Simpson et al. 2019). We also include Spitzer/MIPS 24 μm from D. B. Sanders et al. (2007) and E. Le Floc'h et al. (2009), far-infrared (FIR) maps from Herschel/PACS+SPIRE (D. Lutz et al. 2011; S. J. Oliver et al. 2012), submillimeter imaging from AzTEC on ASTE (I. Aretxaga et al. 2011), and radio maps with the VLA at 1.4 and 3 GHz (E. Schinnerer et al. 2010; V. Smolčić et al. 2017b). As described in the following section, we supplement these wide-area extragalactic data sets with archival pointed ALMA observations between 850 and 1250 μm.

3. Sample Selection

We construct our sample beginning with a $S_{850\,\mu\mathrm{m}} > 2$ mJy source catalog from S2COSMOS (J. M. Simpson et al. 2019). Given the inhomogeneous S2COSMOS field depth between $\sigma_{850} \sim 0.5$ and 1.4 mJy, a flux-limited selection of 2 mJy corresponds to 1985 sources with $\mathrm{SNR}_{850} > 3.5$. Next, we require overlap with the 0.54 deg^2 COSMOS-Web NIRCam area, which contains 706 SCUBA-2 sources with $S_{850\,\mu\mathrm{m}} > 2$ mJy. Of these, 60% have $\mathrm{SNR}_{850} \in [3.5, 5]$, with the remaining 40% having $\mathrm{SNR}_{850} > 5$.

The SCUBA-2 point-spread function (PSF) has an FWHM of 14.″9, which allows for many JWST sources per SCUBA-2 beam. Methods using NIRCam colors to identify SCUBA-2 counterparts have had some success (e.g., S. Gillman et al. 2023) but can still miss the true source of the dust emission. The only way to unambiguously associate SMGs with their multiwavelength counterparts is with high-resolution follow-up using a millimeter interferometer like ALMA, SMA, or NOEMA (Y. D. Hezaveh et al. 2013; J. A. Hodge et al. 2013; A. Karim et al. 2013; D. Brisbin et al. 2017; U. Dudzevičiūtė et al. 2020; J. M. Simpson et al. 2020) or a radio interferometer like the VLA (S. C. Chapman et al. 2005; M. Talia et al. 2021), although a significant number of SMGs can go undetected in deep radio maps (S. C. Chapman et al. 2003; A. J. Barger et al. 2007) or the radio emission can misidentify the counterpart (J. A. Hodge et al. 2013; F. X. An et al. 2018). Therefore, our second selection criterion is the presence of an archival ALMA observation within the FHWM of the SCUBA-2 source in a band well matched to the SCUBA-2/850 μm filter (i.e., Bands 6, 7, and/or 8 between 600 and 1250 μm). We intentionally omit SMG follow-up using lower-frequency ALMA bands, which are explored by J. A. Zavala et al. (2021) and A. S. Long et al. (2024; B4/2 mm blank field selection), O. R. Cooper et al. (2022) and O. R. Cooper et al. (2025, in preparation; pointed B4/2 mm follow-up), and F. Gentile et al. (2025, in preparation; VLA/3 GHz sources). These lower-frequency follow-up techniques can impose different redshift selection functions that may not uniformly capture SCUBA-2 sources (e.g., C. M. Casey et al. 2018). In any case, ∼ 90% of the archival ALMA data over COSMOS are in Bands 6 and 7, so the exclusion of other bands does not exclude a significant fraction of sources. The vast majority of the ALMA coverage comes from Bands 6 ($\lambda_{\mathrm{obs}} \sim 1250$) and 7 ($\lambda_{\mathrm{obs}} \sim 850\,\mu$m), and our final sample is drawn exclusively from observations in these bands, with 97 pointings in Band 6 and 168 in Band 7.

4. ALMA Data Reduction and Fluxes

Using the ALMA archive, we download all observations in Bands 6 and 7 with footprints that overlap a SCUBA-2 source interior to the COSMOS-Web NIRCam area, which totals 265 pointings, 10 of which have pointing centers within 5″ of one another. These ALMA data cover 260 unique S2COSMOS sources. We froze our archival analysis in 2023 November, and so our data set reflects all observations publicly available on the archive as of 2023 September 7. Updating the archival search based on public data as of 2024 July would increase the number of ALMA pointings by 7%, which we leave to future work. We uniformly reimage all of the observations as individual pointings using `tclean` and natural weighting in continuum mode with `CASA v6.6.3` (J. P. McMullin et al. 2007). The angular resolutions among these data range between 0.″022 and 1.″76, with a median of 0.″83 and upper and lower quartiles of 0.″36 and 1.″24, respectively. Only one source was observed in a baseline configuration with resolution below 0.″1. The noise properties across the ALMA data are fairly uniform given the modest rms used when following up single-dish SMGs, and given the fact that 41 of the ALMA observations used in this work come from PID: 2013.1.00118.S (D. Brisbin et al. 2017) and 85 from

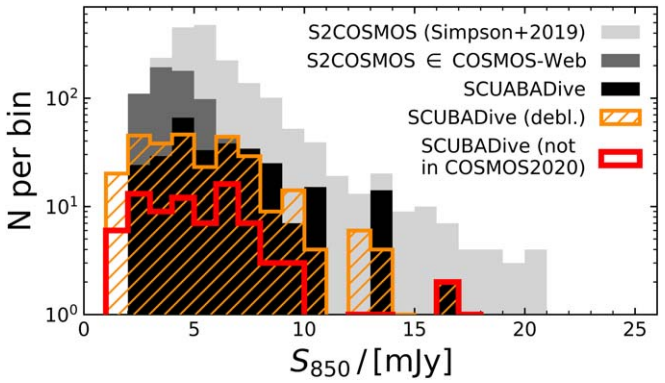

Figure 1. JCMT/SCUBA-2 flux distribution for the parent sample S2COSMOS from J. M. Simpson et al. (2019) and its overlap with the COSMOS-Web footprint. We find ALMA matches for 219 SCUBA-2 sources (black), which corresponds to 289 individual galaxies that compose the SCUBADive sample (orange). Of these, 80 had no prior rest-frame optical/NIR counterpart (i.e., a detection in the COSMOS2020 catalog; J. R. Weaver et al. 2022), as shown in red.

PID: 2016.1.00463.S (AS2COSMOS; J. M. Simpson et al. 2020). The median 1σ map noise is 0.14 mJy, with upper and lower quartiles of 0.08 and 0.19 mJy, respectively.

For ALMA pointings from the AS2COSMOS program we adopt the source list and associated flux densities reported in J. M. Simpson et al. (2020), who perform a thorough search for all submillimeter sources in their Band 7 observations of the brightest ($S_{850} > 6.2$ mJy) SCUBA-2 sources in S2COSMOS. This yields 85 ALMA sources. For all other pointings we conduct a blind source extraction using `PyBDSF` (N. Mohan & D. Rafferty 2015), which was developed and optimized for radio interferometer data. Given that our final sample will include multiple ways to validate counterpart identification, we use the following strategy with `PyBDSF` to consider all tentative ALMA detections as potentially real sources. We first run `PyBDSF` blindly on the non-primary-beam-corrected maps with a 3σ integrated flux threshold and a 4σ peak flux threshold. Then, we rerun `PyBDSF` on the primary-beam-corrected ALMA maps using the last iteration for positional priors and to measure primary-beam-corrected fluxes. In this manner, we identify another 255 $>4\sigma$ candidate ALMA sources that may correspond to SCUBA-2/850 μm emission and an optical counterpart.

From this list we visually check the data comparing the ALMA continuum observations with multiwavelength maps. Out of this initial `PyBDSF` catalog we remove 50 candidate sources that all have integrated and peak ALMA signal-to-noise ratios (SNRs) below 5 and no obvious counterparts in the JWST data. While there is some evidence for "JWST-dark" ALMA sources from S. Fujimoto et al. (2023), these have only been documented in cluster lenses with magnification factors $\mu > 2$. Given the total area of the ALMA data we consider (60.43 arcmin^2) and their individual resolution, we expect to find roughly tens of $4 <$ SNR < 5 noise peaks due to random chance alone. This is basically consistent with the number of SNR < 5 ALMA candidates that have no JWST counterpart and supports the interpretation that these are likely spurious sources.

For spatially resolved sources we adopt an integrated flux density that encases the extent of the source, and for unresolved sources we adopt the peak flux. A minority of sources in the sample are resolved (10%), with most being unresolved point sources. Five sources in our sample have ALMA imaging at 850 μm that likely resolves out extended emission: AzTEC8_0, z23_89_0, z23_74_0, z23_62_0, and z23_62_2. These sources have SNR $= 6-13$ in SCUBA-2 from J. M. Simpson et al. (2019), and the ALMA detections recover $<30\%$ of the deblended SCUBA-2 flux. For these five sources we do not include the ALMA data in any model fits, but the sources are included in the sample, as the ALMA detections identify robust JWST counterparts.

Of the 260 SNR > 3.5 S2COSMOS sources matched to archival ALMA data, we successfully uncover ALMA+JWST counterparts for 219. This includes 96% of SCUBA-2 SMGs with SNR > 5. We do not have counterparts for the remaining 41 SMGs because the associated ALMA data lack detections. This is principally because (a) the S2COSMOS target has SNR < 5 (28/41) and may be spurious to begin with (see J. M. Simpson et al. 2019, Section 3.2) and/or (b) the archival ALMA data are centered $>7''$ from the S2COSMOS peak (10/41), in which case the flux is pushed to the wings of the ALMA primary beam, where the noise is higher. Ten of the unmatched S2COSMOS targets do have SNR > 5 and ALMA pointings centered on their peaks, in which case the ALMA nondetections are surprising. Of these, most are from snapshot programs with integrations of $<2-3$ minutes that could be too shallow for a detection if the SCUBA-2 source is a blend of multiple fainter objects. In any case, these represent a small fraction of our final sample, and future ALMA observations may be needed to secure counterparts to these SMGs.

Our final sample includes 290 sources, corresponding to 289 galaxies and accounting for one doubly imaged lensed source. These galaxies correspond to 219 SCUBA-2/850 μm sources. Of these SCUBA-2 sources, 54 host multiples where two to four ALMA sources contribute to the observed 850 μm emission. Of these, nine SCUBA-2 sources (4% of the total) host triplet submillimeter systems, and 44 (20%) host doublets. One source is resolved into four components all at $z = 2.5$ as originally discussed in T. Wang et al. (2016b). Therefore, we measure a multiplicity fraction for the SCUBA-2 sources of 25%. This is fairly common for follow-up programs of SMGs (C.-C. Chen et al. 2013; Y. D. Hezaveh et al. 2013; J. A. Hodge et al. 2013; A. Karim et al. 2013; D. Brisbin et al. 2017; J. M. Simpson et al. 2020).

A significant fraction of the galaxies in our sample (81/289 = 28%) have no counterpart in the COSMOS2020 catalog within $1''$, which is expected given that 20%–30% of SMGs in pre-JWST studies had no optical/near-IR (OIR) counterpart in the deep field OIR data ($5\sigma \sim 25-26$ mag) prior to JWST (J. L. Wardlow et al. 2011; J. M. Simpson et al. 2014; M. Franco et al. 2018; U. Dudzevičiūtė et al. 2020). Figure 1 shows the final catalog's SCUBA-2 flux distribution, which has an average $\langle S_{850} \rangle$ from SCUBA-2 of $5.9^{+1.9}_{-2.2}$ mJy. A two-sample Kolmogorov–Smirnov test of the SCUBA-2 source flux distribution of SCUBADive versus all S2COSMOS sources in COSMOS-Web returns a Kolmogorov–Smirnov D-statistic and $\log p$ value of 0.3 and -14.8, respectively, which does not reject the null hypothesis that the samples are drawn from different distributions.

4.1. Naming Scheme

There are many options for naming sources in SCUBADive that reflect the data sets used in this work. We choose to preserve the ALMA source name listed in the ALMA science

archive to make it easy for readers to acquire those data. For sources in AS2COSMOS (J. M. Simpson et al. 2020) we adopt their naming scheme directly. All other sources have their ALMA source names appended by an underscore and a number that follows from our source extraction using `pyBDSF` and internal naming schemes therein. For example, the ALMA observation targeting "DSFGS2.60" from PID no. 2015.1.00568.S (PI: Casey) reveals three separate sources that in this work are labeled as DSFGS2.60_0, DSFGS2.60_1, and DSFGS2.60_2.

4.2. Notable Sources

A handful of sources in our catalog are worth mentioning individually given their unique nature and discussion in prior works. AzTECC71 from J. McKinney et al. (2023b) is an SMG at $z_{\rm phot} = 5.7 \pm 0.6$ and in this work is labeled AzTECC71_1. MAMBO-9 (S2COSMOS.850.50_1 in this work) is composed of a pair of unlensed dusty star-forming galaxies at $z_{\rm spec} = 5.850$ (C. M. Casey et al. 2019; S. Jin et al. 2019; H. Akins et al. 2025, in preparation) residing in an overdensity plausibly representing a protocluster environment (M. Brinch et al. 2024). AzTECC3a is a well-known lensed galaxy at $z = 4.6237$ (D. Brisbin et al. 2017; O. Miettinen et al. 2017; N. Álvarez Crespo et al. 2021), with the two counterpart images denoted AzTECC3a_0 and AzTECC3a_1 in this work. J1000+0234_1 is a known dusty star-forming galaxy at the center of an overdense environment and Lyα blob (V. Smolčić et al. 2017a; M. Solimano et al. 2024). AzTEC-2 (in this work AzTECC2b_0) is a pair of massive galaxies at $z_{\rm spec} = 4.633$ making up one of the brightest SCUBA-2 sources in COSMOS (E. F. Jiménez-Andrade et al. 2020; J. M. Simpson et al. 2020; I. Mitsuhashi et al. 2021). AS2COS0005.1 is a lensed SMG at $z = 2.625$ (S. Jin et al. 2024; J. Pearson et al. 2024). Other sources have been reported and studied in prior works but are slightly less well characterized than those mentioned here (e.g., I. Aretxaga et al. 2011; C. M. Casey et al. 2013; J. E. Geach et al. 2017).

5. Multiwavelength Photometry

5.1. Custom Optical/Near-IR Aperture Photometry with `Diver`

The NIRCam counterparts to millimeter/submillimeter-selected galaxies can exhibit complex morphologies that are not optimally captured by classical photometric methods. We tested circular and elliptical apertures from `SE/SE++` (E. Bertin & S. Arnouts 1996) and found (i) many examples where the apertures could not encase the extent of the source without adding in substantial noise, (ii) JWST fluxes inconsistent with ground-based maps at lower resolution, and (iii) generally underestimated flux uncertainties relative to what we expect from the map depths (C. M. Casey et al. 2023a). In light of these challenges, we developed `diver`—an empirically motivated photometry tool built to preserve the resolution of JWST when measuring PSF-matched multiwavelength photometry. We now summarize the methodology of `diver`, which we use to extract optical/near-IR photometry from the u band up to MIRI/F770W and Spitzer/IRAC Channel 4 from both ground- and space-based imaging.

For each of our sources `diver` proceeds through the following: First, we make $50'' \times 50''$ cutouts (to ensure robust noise estimates) around the target in the science image and error/weight image from which a flux will be measured. In this case we use JWST/NIRCam and MIRI data from COSMOS-Web (F115W, F150W, F277W, F444W, F770W) and PRIMER (GO no. 1837; PI: Dunlop; J. S. Dunlop et al. 2021; imaging in F090W, F200W, F356W, F410M) where available, as well as all multiwavelength imaging data compiled in the COSMOS field in COSMOS2020 (e.g., CFHT, HSC, HST, UVISTA, Spitzer; see J. R. Weaver et al. 2022 and Table 1). In principle, any data map can be included in `diver` if accompanied by a PSF and an error map. Next, we identify the reddest NIRCam band containing the source (typically F444W) and create a segmentation map using `photutils` (L. Bradley et al. 2023), in some cases with an additional deblending step included to isolate the source from its neighbors. We save the arbitrarily shaped segmentation boundary down to an SNR per pixel of 3, 5, or 10 as the

Table 1
Table Content of SCUBADive Continuum Data

Instrument/Telescope	Band/Central λ	Units
Ground based:		
MegaCam/CFHT*	u	mJy
HSC/Subaru*	g	mJy
HSC/Subaru*	r	mJy
HSC/Subaru*	i	mJy
HSC/Subaru*	z	mJy
VIRCAM/VISTA*	Y	mJy
VIRCAM/UltraVISTA*	J	mJy
VIRCAM/UltraVISTA*	H	mJy
VIRCAM/UltraVISTA*	K_s	mJy
Band 7/ALMA	850 μm	mJy
SCUBA-2/JCMT	850 μm	mJy
AzTEC/ASTE	1100 μm	mJy
Band 6/ALMA	1150 μm	mJy
Band 6/ALMA	1250 μm	mJy
VLA	S/3 GHz	mJy
VLA	L/1.4 GHz	mJy
Space based:		
ACS/HST*	F814W	mJy
NIRCam/JWST*	F090W	mJy
NIRCam/JWST*	F115W	mJy
NIRCam/JWST*	F150W	mJy
NIRCam/JWST*	F200W	mJy
NIRCam/JWST*	F277W	mJy
NIRCam/JWST*	F356W	mJy
NIRCam/JWST*	F410M	mJy
NIRCam/JWST*	F444W	mJy
MIRI/JWST*	F770W	mJy
IRAC/Spitzer*	Ch. 1	mJy
IRAC/Spitzer*	Ch. 2	mJy
IRAC/Spitzer*	Ch. 3	mJy
IRAC/Spitzer*	Ch. 4	mJy
MIPS/Spitzer	24 μm	mJy
PACS/Herschel	100 μm	mJy
PACS/Herschel	160 μm	mJy
SPIRE/Herschel	250 μm	mJy
SPIRE/Herschel	350 μm	mJy
SPIRE/Herschel	500 μm	mJy

Note. This table is published in its entirety including measurements from all ground- and space-based photometric bands from the optical through radio with their uncertainties, in machine-readable format. Photometry extracted with diver.

(This table is available in its entirety in machine-readable form in the online article.)

custom aperture through which to measure all multiwavelength photometry. Due to the larger PSF, the flux density is generally the most extended in F444W, making it a good choice for capturing the source flux with minimal added noise across bands.

When measuring flux through `diver`'s nonparametric aperture, we make the following calculations to preserve PSF information and properly estimate uncertainties. For maps of poorer spatial resolution than NIRCam/F444W we calculate a PSF correction factor by first convolving the map used for segmentation (F277W or F444W) to the lower resolution using a convolutional PSF kernel derived using `pypher` (A. Boucaud et al. 2016). We take the ratio of the total convolved flux to the convolved flux interior to the custom aperture as our PSF correction factor, effectively using an empirical model of the source from JWST/NIRCam to estimate flux loss from beam smearing in lower-resolution optical/near-IR maps. Then, we measure the flux of the map by summing pixels within the arbitrarily shaped aperture multiplied by this PSF correction factor. To estimate flux errors, we follow the uncertainty in the CCD-based detector given by

$$\begin{aligned}\sigma^2_{\rm aper} &= n_{\rm pix}\sigma^2_{\rm bg} + (\sigma^2_p + \sigma^2_{\rm dark} + \sigma^2_R) \\ &\approx \sigma^2_{\rm boot,sci} + \sigma^2_{\rm boot,err} \end{aligned} \quad (1)$$

for an aperture containing $n_{\rm pix}$ pixels, a background noise of $\sigma_{\rm bg}$ (which we estimate locally), a CCD with shot noise σ_p, and further error terms from dark current ($\sigma_{\rm dark}$) and readout (σ_R). We bootstrap the sky noise ($\sigma_{\rm boot,sci}$) and detector level uncertainties ($\sigma_{\rm boot,err}$) by projecting the science map (after source masking) and error/weight maps, respectively, through the custom aperture randomly placed 1000 times within the $50'' \times 50''$ cutout. We combine these terms in quadrature for a full representation of the flux uncertainty.

For consistency we test the `diver` photometry on targets with simple morphologies (compact sources) by comparing against photometric extraction using `SE/SE++`. For these, the fluxes and flux errors measured with `diver` are generally consistent with the aperture fluxes from `SE/SE++` within $1\sigma_{\rm diver}$, but not within $1\sigma_{\rm SE/SE++} \ll \sigma_{\rm diver}$. Most notably, the multiwavelength fluxes from `diver` are far more consistent between ground-based and JWST data given the expected shape of the rising SEDs into the NIR. Our approach to PSF corrections using the NIRCam light profile and convolutional kernels from `pypher` grounds the multiwavelength photometry estimator in the most accurate empirical model available. One caveat is that this technique assumes that the F277W or F444W light profile is a good model across the full optical/near-IR spectrum, which may or may not be the case; however, it does seem to work well for the purposes of estimating aperture corrections.

Figure 2 shows, for one source, the JWST/NIRCam red-green-blue (RGB) from the COSMOS-Web bands alongside cutouts for most but not all of the optical/near-IR data for which we measure flux densities. We also highlight a system with complex morphology for which `diver` is exceptionally well suited for measuring optimal flux densities.

5.2. X-Rays

We check for X-ray detections of our sources in the Chandra COSMOS Legacy Survey (F. Civano et al. 2016; S. Marchesi et al. 2016). There are 18 SNR > 5 X-ray counterparts to galaxies in SCUBADive with median ($\pm$16th–84th percentiles) $\log L_{2-10\,\rm keV}/({\rm erg\ s^{-1}}) = 43.9^{+0.3}_{-0.5}$. We check for $3\sigma-5\sigma$ detections at the positions of SCUBADive galaxies not found in the X-ray catalogs and find marginal detections for a further ~20% of the sample.

5.3. Optical/Near-IR Aperture Photometry for NIRCam Point Sources

A small subset of SCUBADive galaxies are dominated by point-source components in NIRCam and/or MIRI. There are seven such sources, for which we measure aperture photometry using circular apertures of $r = 0\farcs5$ and make the appropriate PSF corrections. Through curve-of-growth analysis an $r = 0\farcs5$ circular aperture was found to maximize the SNR.

All seven of the point-source-dominated SCUBADive galaxies are detected in X-rays, which indicates the presence of a heavily dust-obscured supermassive black hole. In extreme cases a heavily obscured active galactic nucleus (AGN) can contribute significantly to the FIR and submillimeter fluxes of IR-luminous galaxies (J. McKinney et al. 2021). We leave a careful analysis of such sources in SCUBADive to future works, in part because better empirical constraint on the mid-infrared continuum is needed to disentangle the contribution of AGN to the SED.

5.4. Mid-IR/FIR, Submillimeter, and Radio Fluxes

For mid-IR up through radio fluxes we first check for $>5\sigma$ matches in existing catalogs within $1''$ of the ALMA dust continuum centroid. We use S-COSMOS for Spitzer/MIPS 24 μm (66 matches; D. B. Sanders et al. 2007; E. Le Floc'h et al. 2009), PEP and HERMES for Herschel PACS and SPIRE (20 and 39 matches; D. Lutz et al. 2011; S. J. Oliver et al. 2012; P. D. Hurley et al. 2017), and the VLA at 1.4 and 3 GHz (55 and 153 matches; E. Schinnerer et al. 2010; V. Smolčić et al. 2017b). For objects without matches to catalogs, we set the flux density to that of the pixel containing our target and set the flux uncertainty to that of the total mosaic and flag the data point as an upper limit for the purposes of modeling. As implemented in J. McKinney et al. (2023b), this can include flux contribution from nearby sources in the Herschel/SPIRE bands, a limiting uncertainty that we let propagate into our SED modeling.

As previously mentioned, 88 ALMA sources in our sample belong to doublets where two ALMA sources contribute to the SCUBA-2 flux. A further 27 sources belong to triplets where three sources contribute to the SCUBA-2 flux and one SCUBA-2 system is composed of four ALMA sources. We take a simple approach to deblending the SCUBA-2 flux by dividing the total among the ALMA sources proportional to the ALMA flux ratios. Nearly two-thirds (56/88) of the multiples have Band 7 870 μm imaging and therefore directly constrain the flux ratios contributing in SCUBA-2. For the other sources we are assuming that the flux ratios at 1100−1200 μm and 850 μm are equal. This only falls apart if (a) the targets have very different redshifts or dust temperatures such that 850 μm probes the cold dust SED peak in one while 1.1 mm remains along the Rayleigh–Jeans (RJ) tail in its companion, (b) the submillimeter spectral index β varies dramatically source to source, and/or (c) the observations resolve out emission disproportionately. The standard deviation among β measured for $S_{850} > 5$ mJy SMGs is $<20\%$ (E. da Cunha et al. 2021;

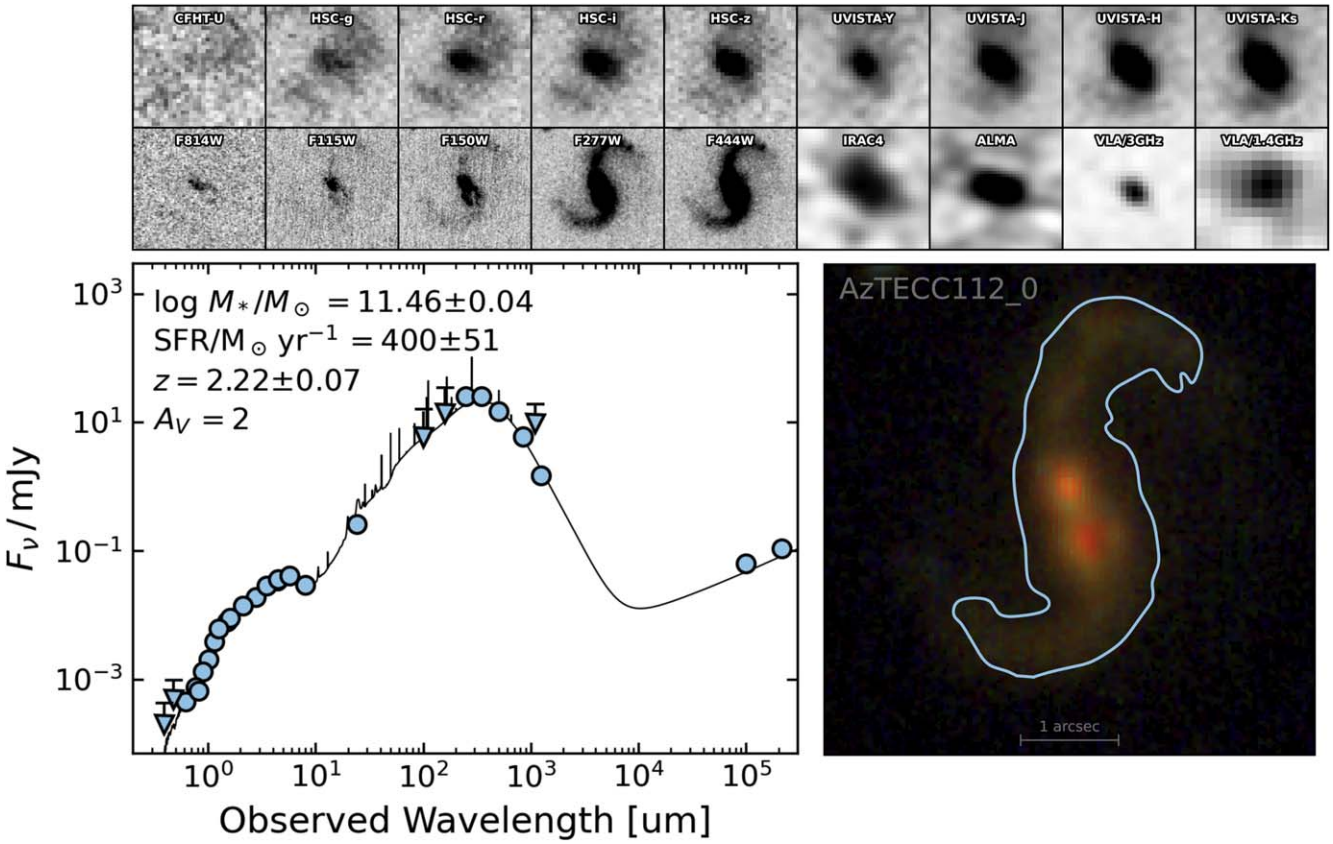

Figure 2. An example of one SCUBADive source in COSMOS-Web and the multiwavelength data we analyze with `diver`. Top: 5″ × 5″ cutouts from COSMOS2020, JWST/COSMOS-Web, ALMA, and the VLA. Bottom left: the optical-through-radio SED, with photometry in blue and the best-fit model in black, and its corresponding best-fit parameters. Bottom right: B = F115W + F150W, G = F277W, R = F444W image of the source AzTECC112_0. Our custom aperture is shown in blue, which we use in the optical through NIR photometry.

O. R. Cooper et al. 2022), which makes this an unlikely source of systematic error in deblending SCUBA-2 emission. No SCUBADive source has $z_{\rm phot} > 6$, beyond which redshift differences would lead to different sampling on and off the RJ tail. Moreover, the cold dust temperatures of submillimeter-detected galaxies appear not to systematically evolve with redshift out to $z \sim 2$ (P. M. Drew & C. M. Casey 2022); however, there is some debate as to how this trend extrapolates to higher redshifts (C. Schreiber et al. 2018; L. Liang et al. 2019; M. P. Viero et al. 2022; L. Sommovigo et al. 2022; H. S. B. Algera et al. 2024), and of course, individual sources can deviate from these trends because of recent starbursts and/or growing supermassive black holes (A. Kirkpatrick et al. 2015). Thus, the cold dust temperature uncertainties constitute a systematic on deblending that only robust FIR SED coverage sampling the peak of the dust continuum can overcome.

6. Derived Quantities

6.1. Spectroscopic Redshifts

We compile spectroscopic redshifts from optical, NIR, and submillimeter/radio spectra for our sources where possible using matches reported in the following: AS2COSPEC (C.-C. Chen et al. 2022b), S. Jin et al. (2019, 2024), B. Horowitz et al. (2022), G. Hasinger et al. (2018), E. A. Shah et al. (2020), F. Valentino et al. (2020), J. S. Kartaltepe et al. (2015), D. Kashino et al. (2019), J. P. Stott et al. (2016), MAGIC (B. Epinat et al. 2024), C. M. Casey et al. (2019), M. Onodera et al. (2015), M. Kriek et al. (2015), QUAIA (K. Storey-Fisher et al. 2024), J. K. Krogager et al. (2014), hCOSMOS (I. Damjanov et al. 2018), zCOSMOS (S. J. Lilly et al. 2007), and zFIRE (T. Nanayakkara et al. 2016). Most of these matches were compiled as part of the latest update to the spectroscopic redshift compilation of all surveys and published redshifts in the COSMOS field (A. A. Khostovan et al. 2025, in preparation). In total we find spectroscopic redshifts for 59 of the 289 galaxies in our sample, with a median $z_{\rm spec} = 2.5$ and 16th–84th percentiles of $z_{\rm spec} = 2.4$ and $z_{\rm spec} = 3.9$, respectively. The highest spectroscopic redshift we include is $z_{\rm spec} = 5.850$ for the well-studied system "MAMBO-9" (C. M. Casey et al. 2019; S. Jin et al. 2019). A majority (60%) of our $z > 3$ spec-z's are from AS2COSPEC (Z. Chen et al. 2021), which uses Band 3 ALMA scans to confirm redshifts of dusty galaxies with multiple CO/[C I] detections. We also measure and report one new $z_{\rm spec} > 5$ from ALMA PID no. 2018.1.00874.S (PI: Oteo) for AzTECC129_0 at $z_{\rm spec} = 5.0175$, based on a detection of CO (4–3) in our rereduction of this archival data set.

6.2. Spectral Energy Distribution Modeling

To derive physical properties across our sample and to estimate photometric redshifts, we fit the multiwavelength photometry listed in Table 1 independently with `CIGALE` (M. Boquien et al. 2019). We assume the following constraints on the model SEDs: a delayed star formation history with a main stellar population of age 0.5−12 Gyr and an e-folding

time $\in$ [30, 6000] Myr, combined with a late-stage burst 50 $-$300 Myr old. We assume a Chabrier IMF (G. Chabrier 2003), solar metallicity, and a modified S. Charlot & S. M. Fall (2000) attenuation curve $\propto \lambda^{-0.7}$ with $A_V \in [0, 9]$. We model the FIR SED using templates from B. T. Draine & A. Li (2007) (as updated in B. T. Draine et al. 2014) with $q_{\rm PAH} \in [0.47, 4]$, a minimum radiation field density $U_{\rm min} \in [5, 50]$, and $dU/dM \propto U^{1-2}$ illuminating $\gamma = 1\%-4\%$ of the dust. We let the redshifts vary between $z = 0.5$ and 7, and we assume a flat prior, unless the target has a spectroscopic redshift, in which case we fix the redshift to $z_{\rm spec}$. Finally, we include a radio power-law component constrained by our VLA 1.4 and 3 GHz data with a fixed slope of 0.8 and FIR/radio correlation coefficient $q_{\rm IR} \in [1.8, 2.6]$ to span the range of values common among high-z, dusty star-forming galaxies (I. Delvecchio et al. 2021). For bands with nondetections we let the models fit the photometry measured through the aperture $\pm$ the 1σ uncertainty. These model and fitting assumptions are successful in reproducing the SEDs of high-redshift, dusty star-forming galaxies as demonstrated by F. Gentile et al. (2024), who also show that they yield results consistent with other modeling codes such as `magphys` (E. da Cunha et al. 2008, 2015; A. J. Battisti et al. 2019), specifically developed for dust-obscured galaxies. We also fit our targets with `magphys` and discuss systematic differences where relevant.

As mentioned in Section 5.3, seven sources have point-like morphologies and X-ray detections indicating that their optical/NIR light might be dominated by an AGN. Out of the remaining sources, $\sim$10% have cataloged X-ray detections from F. Civano et al. (2016) and S. Marchesi et al. (2016). This is consistent with X-ray detection statistics among SMGs from works using much deeper X-ray data than COSMOS (e.g., S. X. Wang et al. 2013), which also find minimal contribution of AGN to the SED. For these reasons we do not believe that AGN are a systematic source of contamination in this sample. Nevertheless, we omit the seven strong X-ray sources with a NIRCam/F444W point-source profile from our population analysis on the stellar masses.

We run the model fits once including all multiwavelength data and then again fitting only to the optical/near-IR photometry up to $\sim$8 μm in MIRI/F770W and/or IRAC 8 μm. The full multiwavelength fit is used when estimating and reporting derived quantities, but we compare against the optical/near-IR fits to assess systematics imposed by `CIGALE`'s energy balance, with particular attention to derived redshifts and stellar masses that are most susceptible to the inclusion of a direct constraint on the dust. As shown in Figure 3, photometric redshifts derived purely from the optical/NIR data are generally lower than those derived from fitting the full multiwavelength SED by $\sim$10%$-$30%. We find that $z_{\rm opt}$ does a better job of recovering spectroscopic redshifts as shown in Figure 3 because of added SED degeneracies in the FIR. Therefore, we adopt $z_{\rm opt}$ as the fiducial photometric redshifts for our sample in the absence of $z_{\rm spec}$. For all other derived quantities we adopt the results from a full multiwavelength fit (with redshifts fixed to $z_{\rm opt}$) including direct constraint on the dust in the FIR and submillimeter. Table 2 lists the redshifts, stellar masses, star formation rates, and A_V we adopt in this paper from our SED modeling.

As a consistency check on our model assumptions, we calculate rest-frame H-band and K-band mass-to-light ratios from the model SEDs, which reflect the stellar ages and star formation history

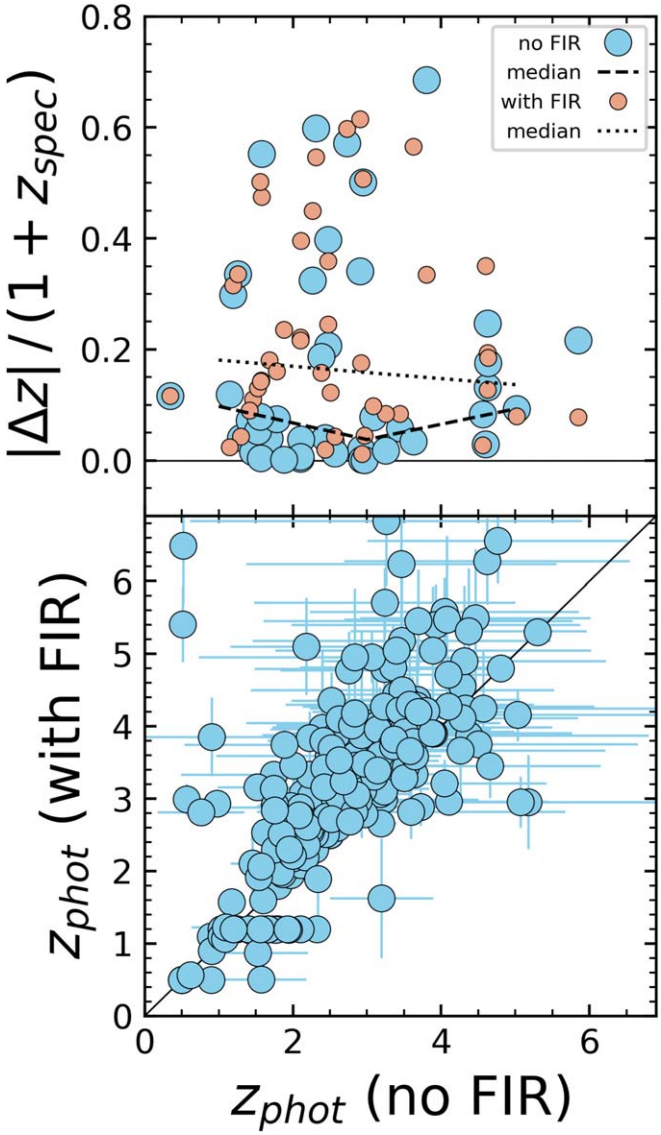

Figure 3. A comparison of photometric redshifts derived using only the optical/near-IR SED up to 8 μm (no FIR) vs. all the multiwavelength photometry out to the radio (with FIR). Top: recovery of spectroscopic redshifts expressed as the fractional deviation $|z_{\rm phot} - z_{\rm spec}|/(1 + z_{\rm spec})$ for both $z_{\rm phot}$ (no FIR; blue) and $z_{\rm phot}$ (with FIR; tan), with binned medians shown as dashed/dotted black lines. Fitting to only the optical/near-IR SED recovers $z_{\rm spec}$ within $\sim$10% out to $z = 6$. Including the FIR data leads to, on average, poorer recovery of $z_{\rm spec}$ to within $\sim$30%$-$40%. Bottom: direct comparison between photometric solutions for $z_{\rm phot}$ (no FIR) and $z_{\rm phot}$ (with FIR). The inclusion of FIR/submillimeter and radio data prefers photometric redshifts that are on average $\sim$30% higher.

(L. J. Hainline et al. 2011; M. J. Michałowski et al. 2014; J. M. Simpson et al. 2014). From the `CIGALE` fits described above we find $\log(M_*/L_H\ [M_\odot/L_\odot]) = -0.33^{+0.37}_{-0.13}$ and $\log(M_*/L_K\ [M_\odot/L_\odot]) = -0.21^{+0.29}_{-0.27}$. The H-band mass-to-light ratio we recover is $\sim$0.2 dex less than the average among ALESS SMGs derived from `magphys` in E. da Cunha et al. (2015), as well as for AS2UDS SMGs in U. Dudzevičiūtė et al. (2020). To account for this artificial offset in mass tied to the different modeling assumptions, and for a fair comparison against the literature, we normalize our stellar masses from `CIGALE` to the average H-band mass-to-light ratio of E. da Cunha et al. (2015).

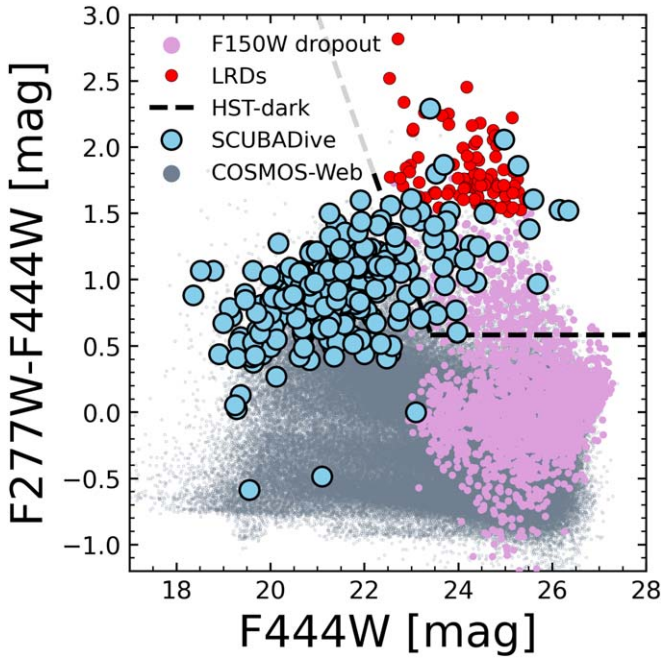

Figure 4. JWST/NIRCam color–magnitude diagram in the F277W and F444W filters for ∼300,000 galaxies in the COSMOS-Web survey with SNR > 10 (gray), the subset with no detection in F150W (pink), SCUBADive (blue), and LRDs (red; H. B. Akins et al. 2024). The dashed black line outlines a typical color–magnitude wedge used to select HST-dark $z \gtrsim 3$ dusty galaxies (e.g., L. Barrufet et al. 2023). SMGs exhibit a redder F277W − F444W color than ∼95% of all sources in COSMOS-Web, and the $z > 3$ SCUBADive subset preferentially has F444W > 23 mag and F277W − F444W > 0.6. The reddest SMGs in SCUBADive also overlap with the domain of LRDs, but they do not qualify for the compactness criterion that reflects LRD point-source morphologies (H. B. Akins et al. 2024). There are 480 F150W dropouts in COSMOS-Web that fall within the high-z, dusty galaxy selection wedge (black dashed line) and do not belong to either the SCUBADive/SMG or LRD samples. These F150W-dropout, red galaxies may represent less extreme counterparts to the SMGs and LRDs in terms of their stellar masses, A_V, and specific star formation rates.

7. Results

7.1. JWST Photometry and NIRCam Colors

Figure 4 shows the NIRCam F277W and F444W color–magnitude space spanned by our sample. SCUBADive SMGs have NIRCam [F444W] < 26.5, in good agreement with predictions from C. d. P. Lagos et al. (2020) and the SHARK semianalytic model. In these filters, SCUBADive galaxies are redder than 95% of all other sources in COSMOS-Web, and the F444W magnitude correlates with the [F277W] − [F444W] color such that fainter sources are redder, consistent with higher redshifts and A_V. Out of the total sample containing 289 galaxies, 157 (54%) are not detected in NIRCam/F115W at SNR > 5, and 78 (27%) are not detected in NIRCam/F150W at SNR > 5, which are explored in detail in S. M. Manning et al. (2025, in preparation). Considering an SNR > 3 threshold, these detection statistics change to 115 (40%) and 60 (21%) for F115W and F150W, respectively. The nondetection rate in F150W ($<5\sigma$) is very similar to the fraction of SMGs that historically have not had optical counterparts or are described as "optically dark" (J. L. Wardlow et al. 2011; J. M. Simpson et al. 2014; M. Franco et al. 2018; U. Dudzevičiūtė et al. 2020), even though the NIRCam/F115W depth is much deeper than the UltraVISTA data at the same wavelength. In SCUBADive these galaxies have $\langle \log M/M_\odot \rangle \sim 11$, $\langle z \rangle = 3.3$, and $\langle A_V \rangle = 3.5$. There are thousands of COSMOS-Web sources with F277W − F444W > 0.5 and no F150W detection, which may also represent $z > 3$ dust-obscured star-forming galaxies (L. Barrufet et al. 2023; see also E. Gammon et al. 2025, in preparation). Only nine sources have SNR < 5 in NIRCam/F277W, one of which is MAMBO-9 at $z = 5.850$ (C. M. Casey et al. 2019), hinting at a rare population of massive and dusty galaxies very faint at 2.7 μm.

A handful of SMGs in SCUBADive exhibit unusual colors. Most are red in [F277W] − [F444W] between 0.5 and 1.5 mag with [F444W] = 20−24 mag, but a small subset ($N = 12$) with [F277W] − [F444W] > 1.5, $z = 3.5-5$, $\log M_*/M_\odot = 11.1 - 12.3$, and $S_{850} = 3-6$ mJy overlap with the NIRCam LW colors of so-called "little red dots" (LRDs). However, the SCUBADive galaxies in this parameter space do not have blue SW slopes, nor do they have 40%–70% of their flux within 0.″2, which is an important compactness criterion for LRD selection (H. B. Akins et al. 2024; see also F. Gentile et al. 2025, in preparation, for discussion of "not so little red dots").

Among the bluer sources in the NIRCam LW bands, 12 SCUBADive galaxies have [F277W] − [F444W] < 0.3 mag, two of which have $z \sim 1$ and low star formation rates $\sim 50\,M_\odot\,\mathrm{yr}^{-1}$ relative to the typical range of SMGs (E. da Cunha et al. 2015). One source in our sample, J1000+0234_1, is unusually blue with [F277W] − [F444W] ∼ 0. As previously mentioned, this source resides within an overdensity at $z = 4.54$. M. Solimano et al. (2024) conduct a NIRSpec/IFU analysis of this source and find very strong [O III] λ5007 with equivalent width >1000 Å that must contribute significantly to its F277W photometry, hence the very blue [F277W] − [F444W] color (e.g., J. McKinney et al. 2023a). The two bluest sources with [F277W] − [F444W] = −0.59 mag make up a foreground galaxy (AS2COS0005.2, $z = 0.5$) and lensed galaxy (AS2COS0005.1, $z = 2.6$) pair. Given the spatial extent of the foreground source, there is likely significant contamination to the background object's NIRCam photometry.

Table 2
Table Contents for Derived Physical Properties in SCUBADive

Column	Units	Description
id	⋯	Source ID
ra	degrees	R.A. J2000
dec	degrees	decl. J2000
z_opt	⋯	OIR photo-z
z_full	⋯	With FIR photo-z
z_spec	⋯	Spec-z
logmstr	$M_\odot$	log stellar mass
sfr	$M_\odot\,\mathrm{yr}^{-1}$	log SFR
Av	mag	Attenuation

Note. This table is published in its entirety including in machine-readable format. We include 1σ uncertainties on derived quantities using the appropriate column names appended by _err.

(This table is available in its entirety in machine-readable form in the online article.)

7.2. NIRCam Morphology

A major advantage of JWST, in addition to its sensitivity, is its unprecedented spatial resolution in the NIR probing the rest-frame optical emission in galaxies at high z. This has enabled recent studies into the substructures of heavily dust-obscured galaxies. W. Rujopakarn et al. (2023) identify stellar substructure in one $z = 2.696$ star-forming galaxy with ALMA

and JWST. Y. Wu et al. (2023) identify spiral arms in an SMG at $z = 3.059$ using NIRCam, and both C.-C. Chen et al. (2022a) and C. Cheng et al. (2022) identify compact reddened substructures in NIRCam maps of several SMGs at $z \sim 2$ with hints of spiral arms and stellar bars. J. A. Hodge et al. (2024) find that the surface density of dust continuum and red NIRCam colors correlate on kiloparsec scales, reinforcing the origin of their red colors in dust obscuration rather than older stellar populations. In an analysis of 80 SMGs S. Gillman et al. (2024) find lower Sérsic indices than less active galaxies of comparable redshift and specific star formation rate, which may indicate lower-mass black holes, lower dynamical stability, and therefore an increase in secular and/or minor merger triggering of star formation in the SMGs.

The Appendix contains the RGB postage stamps for our sample. We visually classify galaxies using uniformly scaled RGBs with two classifiers (JM, CS). We identify 50 ± 7 (17% ± 4%) SMGs with disturbed morphologies, evidence of an ongoing or recent major merger. This occurrence of mergers is consistent with the morphology analysis of S. Gillman et al. (2024). A further 32 ± 5 (11% ± 3%) SMGs exhibit spiral arms, and 23 ± 6 SMGs (8% ± 3%) show evidence for stellar bars. The remaining sources are either compact and smooth (∼40%) or clumpy (∼20%). We investigate the candidate stellar bars further by subtracting out a 2D Sérsic profile fit to the central bulge emission in F444W to reveal underlying structure and also by modeling the radial profile with a series of 2D ellipsoids as described in Y. Guo et al. (2023). This corroborates the evidence for 10 bars and leaves the rest as candidates.[42] The barred structures of SCUBADive sources will be explored in further detail in future works (C. Silva et al. 2025, in preparation). For now, we show in Figure 5 examples of stellar bars in SMGs, including one source at $z = 3.4 \pm 1.3$ that if verified would be the highest-redshift stellar bar detected to date. I. Smail et al. (2023) also report a candidate stellar bar in a $z = 4.26$ SMG, suggesting that massive and obscured sources may be sites of early bar onset. One interesting source to note is z23_10_0, which has clear spiral arms and a point-source F444W component in the nucleus. After subtracting a point-source model, there is tentative evidence for a stellar bar, suggesting that gas can still feed a central AGN despite the resonance trapping imposed by bars. The fact that (1) the fraction of SMGs exhibiting bars and/or spirals is about equal to those exhibiting disturbed morphologies and (2) most SMGs have smooth morphologies means that major mergers cannot be invoked to fully explain the submillimeter-bright starburst phase (P. F. Hopkins et al. 2008) and that in situ mechanisms for extreme gas compaction are certainly at work (J. A. Hodge et al. 2016). This is consistent with S. Gillman et al. (2024) and also the results of submillimeter imaging that find a high incidence of disklike morphologies in SMGs (L. L. Cowie et al. 2018; B. Gullberg et al. 2019; J. A. Hodge & E. da Cunha 2020).

7.3. Redshifts

The redshift distribution of SMGs has been the focus of many works dating back to the earliest spectroscopic follow-up campaigns at optical (S. C. Chapman et al. 2003, 2005) and radio (A. Weiß et al. 2009) wavelengths. Among SMGs with $S_{850} \gtrsim 1$ mJy the field has mostly converged $\langle z \rangle \sim 2.5$, with lower and upper quartiles of $z = 1.8$ and $z = 3.4$, respectively (e.g., E. da Cunha et al. 2015; D. Brisbin et al. 2017; J. M. Simpson et al. 2019; U. Dudzevičiūtė et al. 2020). As shown in Figure 6, we recover this range with a median $z = 2.6$ and lower/upper quartiles spanning $z = 1.6$–3.5. However, a subset of SMGs with no optical counterparts (prior to JWST) have had highly unconstrained redshifts (C. M. Casey et al. 2018; M. Franco et al. 2018). ALMA follow-up has revealed that they overwhelmingly have $z_{\rm spec} \gtrsim 3$ (Z. Chen et al. 2021), but such confirmation usually requires >1 hr per source to complete a full Band 3 scan. With JWST we can now derive well-constrained photometric redshifts for sources that have not been detected by prior ground- and space-based maps. For the SCUBADive sources with no counterparts in COSMOS2020 (i.e., having lacked a secure optical source until now) we find a median z and upper/lower quartiles of $\langle z \rangle = 3.1^{+1.2}_{-1.3}$, with 26% having $z > 4$. Remarkably, the fraction of sources with no prior optical/near-IR counterpart before JWST is ∼20% between $1 < z < 3$ (Figure 6(b)). These galaxies have $A_V \in [1, 4]$ with $\langle A_V \rangle = 2$ and $\langle \log M_\odot/M_* \rangle = 11.3$, demonstrating that even massive systems at lower redshift have eluded optical detection because of their dust attenuation. At $z > 4$ the fraction of sources with no prior optical/near-IR counterpart grows to 75%.

7.4. Stellar Masses

Due to their high attenuation and likely stochastic star formation histories, the stellar mass distribution of SMGs has been difficult to assess and impossible to measure for the ∼30% of SMGs that have had no optical counterpart prior to JWST. In fact, the stellar masses among the same samples of highly dust-obscured galaxies can change by up to an order of magnitude depending on assumptions and the available data (L. J. Hainline et al. 2011; M. J. Michałowski et al. 2012). Here we report the stellar mass statistics measured for our sample and compare to previous works in the literature. Note that in this section (and throughout the rest of this work) we consider the stellar masses after applying the mass-to-light ratio correction factor discussed in Section 6.2.

The median stellar mass in our sample is $\log M_*/M_\odot = 11.1^{+0.3}_{-0.5}$ and spans the range $\log M_*/M_\odot = 9$–12.2. The average 1σ stellar mass uncertainty from our model fits is $0.07^{+0.11}_{-0.04}$ dex, which is less than the 0.1 dex systematic variance of stellar masses from the choice of star formation history (e.g., A. C. Carnall et al. 2019). Our median mass is greater than that of canonical analyses of SMGs by ∼0.2 dex (e.g., C. Borys et al. 2005; L. J. Hainline et al. 2011; M. J. Michałowski et al. 2012). More recently, ALMA has been used to identify counterparts to SMGs in deep NIR maps and HST images, which have led to revised stellar mass measures. As shown in Figure 7, the stellar mass distribution of SCUBADive is fully consistent with AS2UDS SMGs from U. Dudzevičiūtė et al. (2020), which were constrained primarily with K-band and IRAC 3.6 μm maps with 3σ depths of 25.7 and 23.5 mag, respectively. The SCUBADive stellar masses are generally consistent with those found for SMGs in the ALESS sample (E. da Cunha et al. 2015), but the median of SCUBADive is 0.3 dex greater than that of ALESS.

Figure 8 shows the change in derived stellar mass for SCUBADive under three different model/data combinations.

[42] (1) Maximum ellipticity $e > 0.25$ along the bar with constant position angle, and (2) a drop in ellipticity of 0.1 or more combined with >10° position angle change over the transition from the bar-dominated region to the outer disk. See also S. Jogee et al. (2004) and I. Marinova & S. Jogee (2007).

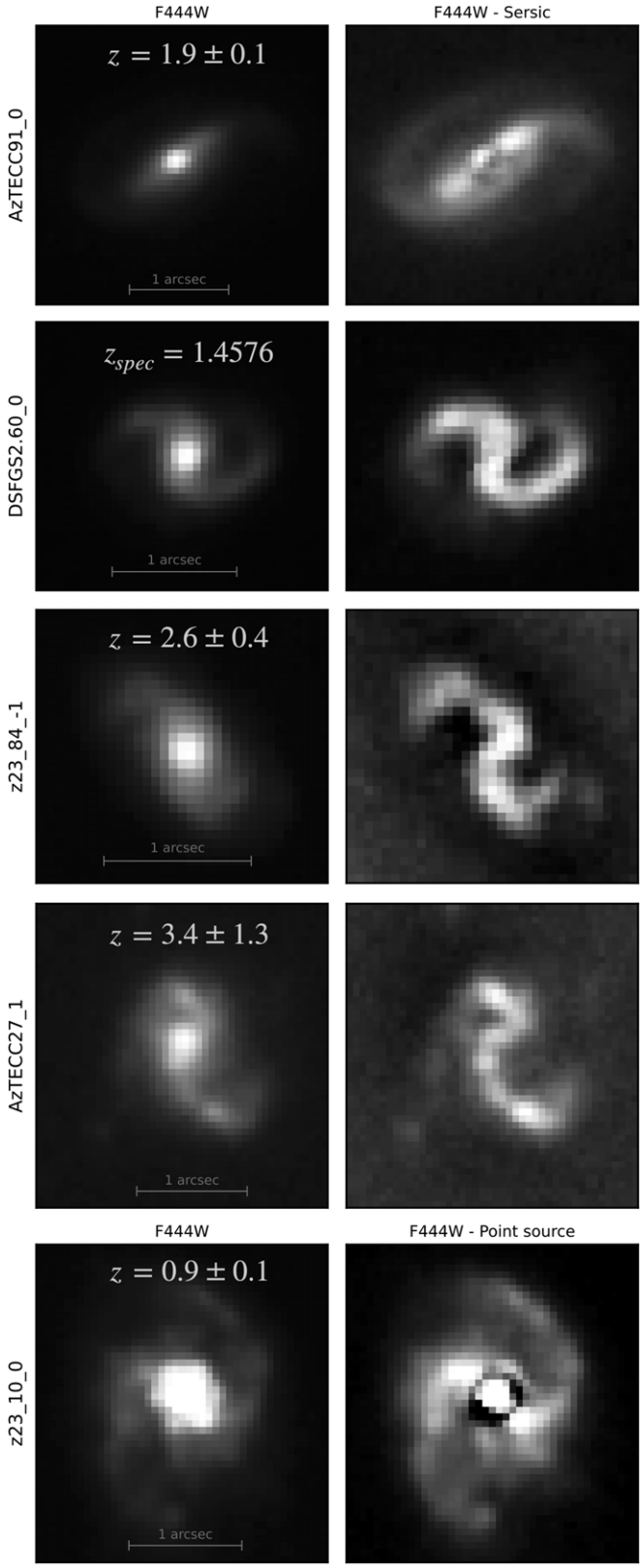

Figure 5. F444W cutouts for SCUBADive sources exhibiting candidate stellar bars, with Sérsic-subtracted F444W maps on the right to reveal the bar and spiral arm structures. In the bottom row we show an SMG hosting a nuclear point source in F444W with a residual also revealing a candidate stellar bar.

First, we compare the masses from the COSMOS2020 FARMER catalog (J. R. Weaver et al. 2022) and our updated masses that include the JWST constraint. There is no systematic offset between these cases; however, sources with masses in COSMOS2020 >0.5 dex away from our derivations were previously fit by models that assumed no dust ($A_V \sim 0$) and underestimated the redshifts by 1.2 on average, with 50% having ($z_{C2020} - z_{SCUBADive}$) < -2. In total, 66 (23%) of the SCUBADive galaxies were significantly misclassified with respect to their stellar mass, A_V, and redshift. The most extreme cases correspond to SMGs misidentified as $z = 0.6-0.8$ dwarf galaxies ($N = 23$, 8%) and $z \sim 0-5$ post-starburst/quiescent galaxies ($N = 14$, 5%) with SFR$/M_* < 10^{-10}$ yr^{-1}. This is unlikely to drastically impact the number density of either interloper population, but it represents a significant fraction of the SMG sample. Figure 8 also compares the stellar masses we estimate using CIGALE versus magphys, which on average agree with with one another as expected given the M_*/L_H correction we implement for consistency with E. da Cunha et al. (2015). The ~0.3 dex scatter in CIGALE versus magphys stellar masses could arise from the internal treatment of attenuation (R. Uematsu et al. 2024, Appendix D), but it most likely reflects lingering effects of the star formation history assumptions between the two models: although we normalize to the mean M_*/L_H of E. da Cunha et al. (2015), both their work and ours exhibit a $1\sigma M_*/L_H$ of 0.2–0.4 dex. Finally, we also rerun the SED fits leaving out MIRI/F770W where available to test how the reddest SED sampling from JWST systematically changes our results. On average the masses do not change if the MIRI data are removed from the fits, and the mass uncertainties only decrease by 1%–7% when fitting includes MIRI/F770W.

7.5. Optical Attenuation

In Figure 9 we show the distribution in A_V as a function of total stellar mass and redshift. SCUBADive has $\langle A_V \rangle = 2.6^{+1.5}_{-1.0}$, which overlaps with the attenuation inferred among SMGs from ALESS (E. da Cunha et al. 2015), as well as the HST-dark NIRCam-selected galaxy sample from L. Barrufet et al. (2023, 2024) that exhibits comparable A_V at ~2 dex lower stellar mass. These samples of dust-obscured galaxies all exhibit higher A_V for fixed stellar mass than the more normal sample of $z \sim 1-4$ galaxies from MOSDEF (M. Kriek et al. 2015; N. A. Reddy et al. 2015; I. Shivaei et al. 2015). Galaxies without a prior counterpart in COSMOS2020 have $\langle A_V \rangle = 3.0^{+2.0}_{-1.5}$, ~25% greater than the median of those with a match in COSMOS2020, and the faintest subset of SCUBADive in F444W with [F444W] > 24 mag has $\langle A_V \rangle = 4^{+1}_{-2}$ and tends to have $z > 3$ as shown in Figure 9 (right). While these A_V measurements are likely uncertain to ~20% with only four NIRCam bands (see J. McKinney et al. 2023b), the submillimeter constraint from SCUBA-2 and ALMA reduces systematic uncertainty pertaining to less obscured solutions. Furthermore, L. Barrufet et al. (2024) confirm with NIRSpec the high $A_V > 2$ for HST-dark galaxies, a likely less extreme population having lower A_V than sources in this work for lack of submillimeter counterparts. The optically faint subset (less than four detections in optical/near-IR photometric bands) of ALESS has $\langle A_V \rangle = 2.9^{+0.3}_{-0.3}$. The added constraint by JWST aids in robustly identifying SMGs with higher A_V and higher redshift but that still exhibit the high stellar masses and star formation rates common among SMGs in general.

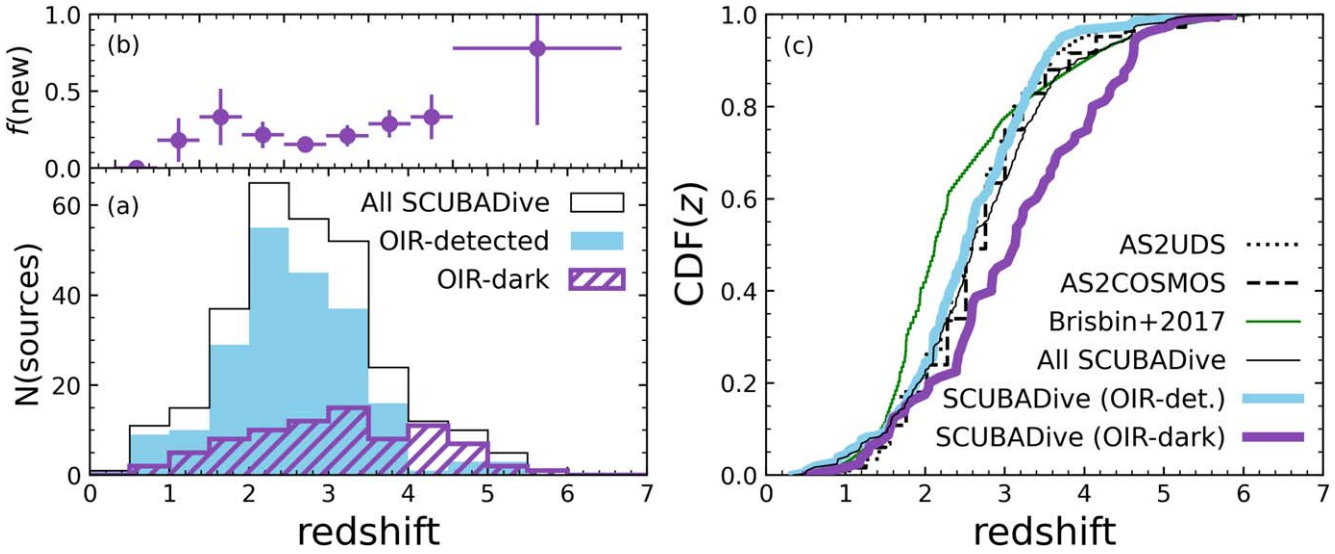

Figure 6. Redshift distributions. (a) The redshift histogram for all of SCUBADive (black), sources that have counterparts in COSMOS2020 (blue), and the "new" OIR-dark subset with no prior counterparts (purple). In panel (b) we show the fraction of NIR-dark sources in SCUBADive between $z = 0$ and 6, which grows from an average of 20% ± 10% at $1 < z < 4$ to nearly 100% at $z > 4$. In panel (c) we compare the SCUBADive cumulative redshift distribution function against large analyses of SMGs: AS2COSMOS (J. M. Simpson et al. 2020), AS2UDS (U. Dudzevičiūtė et al. 2020), and D. Brisbin et al. (2017). SCUBADive is consistent with these prior works, and the OIR-dark subset is biased toward higher redshifts.

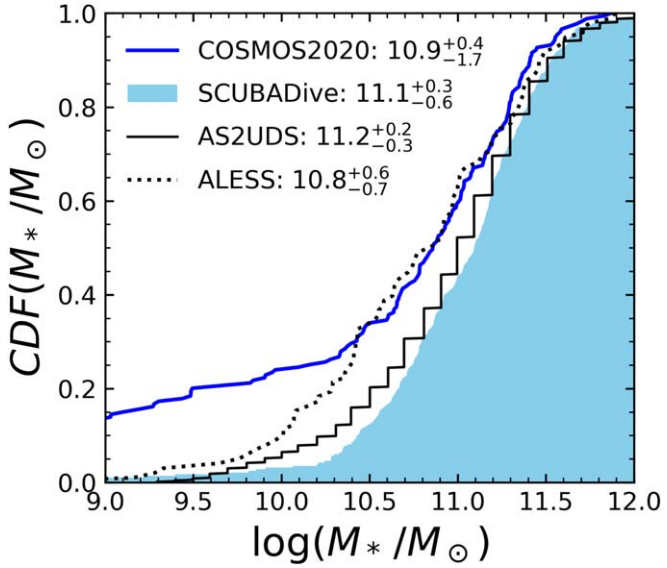

Figure 7. Stellar mass cumulative distribution function for SCUBADive (blue shaded region) compared to the AS2UDS (U. Dudzevičiūtė et al. 2020) and ALESS (E. da Cunha et al. 2015) samples of SMGs. We report the 16th, 50th, and 84th percentiles for each distribution. The mass cumulative distribution function for SCUBADive prior to JWST (i.e., from COSMOS2020; J. R. Weaver et al. 2022) is shown with a dashed blue line.

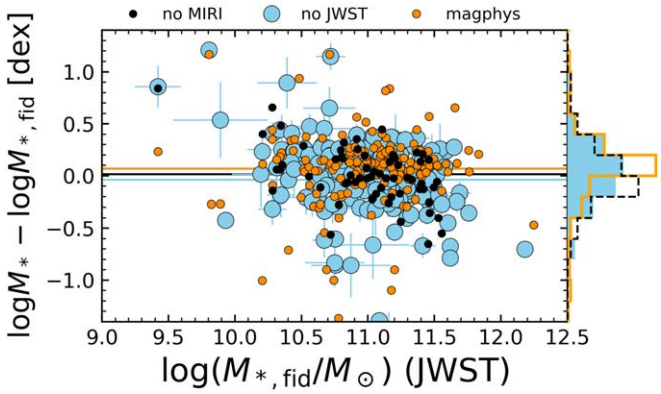

Figure 8. The difference in stellar masses derived for our sample under various modeling assumptions and data inclusion. Our fiducial stellar mass ($M_{*,\mathrm{fid}}$) refers to the CIGALE fits outlined in Section 6.2 normalized to the H-band mass-to-light ratio (E. da Cunha et al. 2015). We show the change in M_* with and without the inclusion of JWST data by comparing against derived stellar masses from the COSMOS2020 FARMER catalog (J. R. Weaver et al. 2022; blue circles). We also compare against M_* inferred from leaving out the JWST/MIRI data from our fits (black) and when using the magphys SED fitting code (orange). The solid lines show the average change in stellar mass for each modeling approach, which are all within 0.08 dex of zero. There is no statistically significant correlation between the mass offset when leaving out JWST data and the total stellar mass as measured by JWST with a Pearson correlation coefficient r_p and p-value of $r_p = -0.21 \pm 0.04$ and $p = 0.03 \pm 0.03$. Note that the number of sources in each mass comparison group is not the same because only 94 have MIRI fluxes and 81 lack COSMOS2020 counterparts. We have cropped the y-axis to avoid showing the 5% of sources misclassified as $z < 1$ dwarf galaxies as discussed in Section 7.4.

8. Discussion

8.1. The Volume Density of SMGs

Most SMGs have $z \sim 1-3$ with an average of $z \sim 2.5$ (S. C. Chapman et al. 2005; F. Walter et al. 2012; E. da Cunha et al. 2015; D. Brisbin et al. 2017; U. Dudzevičiūtė et al. 2020; J. M. Simpson et al. 2020) and a high-end tail at $z > 3-4$ associated with those lacking optical counterparts (e.g., M. Franco et al. 2018; C. C. Williams et al. 2019; S. M. Manning et al. 2022). The $z > 3$ subset of the SMG population has been of growing interest as (a) models of dust formation in the early Universe demonstrate how difficult creating early dust reservoirs might be (C. Gall et al. 2011; G. Popping et al. 2017) and (b) they are good progenitor candidates for the emergent $z \sim 3$ quiescent galaxy population (S. Toft et al. 2014; A. S. Long et al. 2023). In both regards, the volume-averaged number density of SMGs is a key measurable that models must reproduce, as it captures the formation history, source density, and duty cycle of $z > 3$ SMGs. Prior to JWST the volume density of $z > 3$ SMGs exhibited over 1 dex in scatter owing to small survey volumes, small number statistics, and highly uncertain photometric redshifts

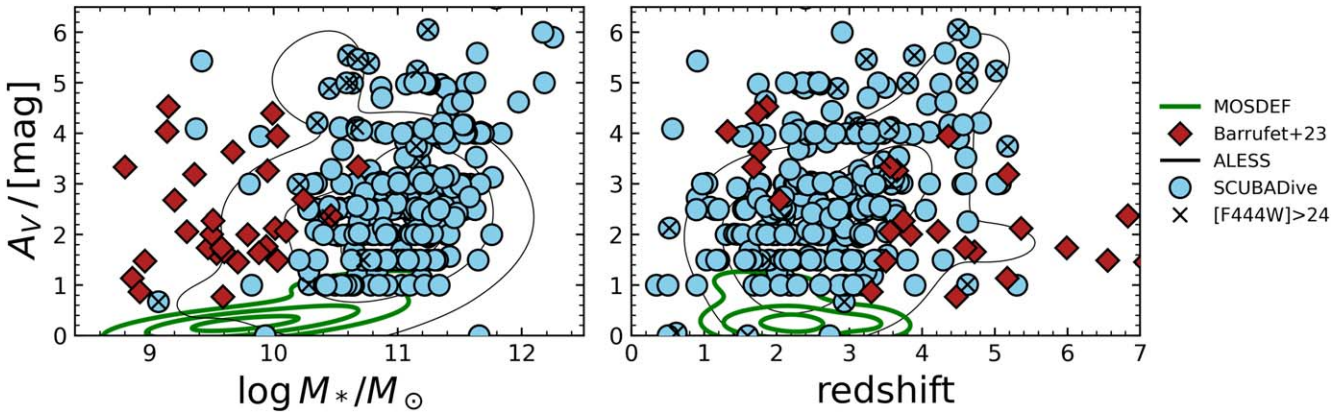

Figure 9. Stellar optical attenuation A_V vs. total stellar mass (left) and redshift (right). SCUBADive is shown in blue compared to normal $z \sim 1-3$ galaxies from MOSDEF (green contours; M. Kriek et al. 2015; N. A. Reddy et al. 2015; I. Shivaei et al. 2015), ALESS SMGs (black contours; E. da Cunha et al. 2015), and the HST-dark sample of L. Barrufet et al. (2023, 2024) as red diamonds. Black crosses indicate SCUBADive sources with [F444W] > 24 mag.

(J. A. Zavala et al. 2021; A. S. Long et al. 2023). Programs like AS2COSPEC (Z. Chen et al. 2021) are making significant progress in this regime, with 52 spectroscopic redshifts for $z > 2$ SMGs in COSMOS; however, spectroscopic follow-up with ALMA is time expensive. Given the significant photometric redshift constraint added by JWST on optically faint sources coupled to the wide area of COSMOS-Web as compared to other JWST extragalactic fields, SCUBADive is well suited to constrain the $z > 3$ volume density of SMGs at high precision.

Figure 10 shows the volume density of SCUBADive SMGs with $\log(M_*/M_\odot) > 10^{10}$ and $S_{850} > 2$ mJy between $z = 1$ and 6 assuming redshift bins of $\Delta z = 1$. We restrict our volume density measurement to SCUBADive sources with deblended $S_{850} > 2$ mJy (87% of total) for completeness reasons. The error bars capture cosmic variance uncertainty, the $\sqrt{N}$ Poisson uncertainty, and the photometric redshift uncertainty, which we fold in by bootstrapping the measurement using 1000 iterations of the sample's redshifts perturbed by their 1σ uncertainties. There are 487 SMGs in the COSMOS-Web area that do not have a secure JWST/NIRCam counterpart for lack of ALMA data. We have corrected for this by scaling the counts in each redshift bin assuming that the SCUBADive redshift posterior applies to the unmatched SMGs. We also correct for the completeness of the SCUBA-2 map, which can be as low as 50% around the SNR limit of the S2COSMOS catalog (J. M. Simpson et al. 2019). A total of 44% of SCUBADive sources correspond to SCUBA-2 sources with $S_{850} > 6.4$ mJy, where the average completeness of the S2COSMOS map is >90% (J. M. Simpson et al. 2019). We estimate a completeness correction factor from the range of SCUBA-2 850 μm flux densities in SCUBADive and the completeness function of J. M. Simpson et al. (2019). On average, this increases the volume density by 0.2 dex at most, and it is worth noting that COSMOS-Web overlaps with the deepest portion of the SCUBA-2 map. Table 3 lists the SCUBADive volume density.

Volume density measurements must be accompanied by proper estimates on their uncertainties attributed to cosmic variance: variation in observed source counts attributable to large-scale density fluctuations (B. P. Moster et al. 2011). This is especially true when discussing favored models and those ruled out by the observations (M. Trenti & M. Stiavelli 2008), and it certainly factors into the $\sim$2 dex range in reported volume densities on $z > 3$ SMGs found in the literature. More often than not the error bars quoted on volume densities

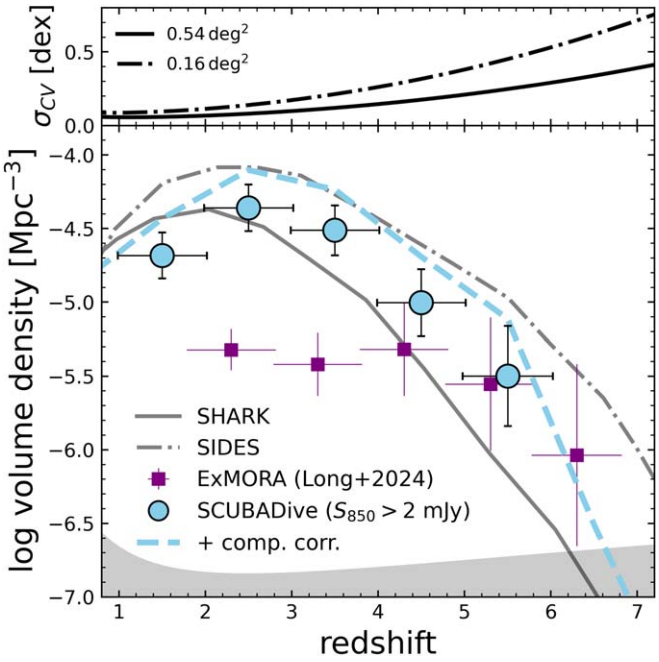

Figure 10. The volume density of dusty star-forming galaxies inferred from SCUBADive (blue circles) out to $z = 6$ in bins of redshift with $\Delta z = 1$. We compare to the semianalytic model predictions of SHARK (gray solid line; C. d. P. Lagos et al. 2019, 2020) and SIDES (gray dashed line; M. Béthermin et al. 2017), as well as results from the 0.16 deg^2 2 mm blank field ExMORA (purple; A. S. Long et al. 2024). The dashed blue line represents the maximal volume density allowed by the completeness of S2COSMOS (J. M. Simpson et al. 2019), and the shaded gray region corresponds to the limit of one source per bin over the COSMOS-Web area. The top panel shows the cosmic variance uncertainty inherent to volume densities by their survey area, assuming bins in redshift of $\Delta z = 1$, stellar masses $>10^{10}\,M_\odot$, and following the formalism in B. P. Moster et al. (2011). We show the 1σ cosmic variance for a 0.54 deg^2 field (e.g., COSMOS-Web) and a 0.16 deg^2 field (e.g., CEERS, ExMORA). Uniform selection over large areas like COSMOS-Web is critical for overcoming the limitations of cosmic variance and for discriminating between galaxy formation models at $z \gtrsim 3$.

only reflect the Poisson statistics of the sample. Here we outline our method for calculating the volume density uncertainty from cosmic variance, which follows the formalism developed by B. P. Moster et al. (2011; see their Section 3.4). First, we start with the dark matter root cosmic variance ($\sigma_{\rm dm}$) reported by B. P. Moster et al. (2011) for the COSMOS field

Table 3
SCUBADive Volume Density over COSMOS-Web for SCUBA-2 Sources with $S_{850} > 2$ mJy, and the Relevant Error Terms from Poisson Noise (σ_p), Cosmic Variance (σ_{CV}), and Redshift Uncertainties (σ_z)

z	$\log(n/\mathrm{Mpc}^3)$	σ_p	σ_{CV}	σ_z
$1 < z < 2$	-4.68 ± 0.15	0.06	0.06	0.13
$2 < z < 3$	-4.35 ± 0.16	0.04	0.08	0.13
$3 < z < 4$	-4.51 ± 0.17	0.05	0.12	0.11
$4 < z < 5$	-5.00 ± 0.23	0.09	0.18	0.11
$5 < z < 6$	-5.50 ± 0.34	0.18	0.25	0.15

Note. These table values have not been corrected for the incompleteness of the parent SCUBA-2 map, which could increase the volume density by 0.2 dex on average in each redshift bin. They have been corrected for the SCUBADive sampling of S2COSMOS SMGs over COSMOS-Web.

(7045 arcmin^2). We next scale this to the area of COSMOS-Web (1944 arcmin^2) by interpolating between σ_{dm} reported for the UDF, GOODS, GEMS, EGS, and COSMOS in B. P. Moster et al. (2011). Next, we calculate the galaxy bias $b(m_*, \bar{z})$ for the stellar mass range in our sample ($>10^{10.5}\,M_\odot/M_*$; see Figure 7) and at the center of each redshift bin ($\bar{z}$), where we calculate a volume density. The bias ranges from 2 at $z = 1$ to 22 at $z = 5$. We next compute the root cosmic variance for galaxies $\sigma_{CV} = b(m_*, \bar{z})\sigma_{dm}(\bar{z}, \Delta z = 0.2)\sqrt{0.2/\Delta z}$. The last term is there to match the redshift bin widths we adopt of $\Delta z = 1$. For comparison we also calculate the galaxy root cosmic variance assuming a field area of 700 arcmin^2 to compare against surveys like CEERS in the EGS and ExMORA in COSMOS. For the COSMOS-Web area and a redshift bin width of $\Delta z = 1$ we estimate σ_{CV} for SMGs to be 0.12 dex at $3 < z < 4$, 0.18 dex at $4 < z < 5$, and 0.25 dex at $5 < z < 6$. For a 700^2 arcmin area the root cosmic variance at $z > 3$ is $\sim$0.3 dex greater in each bin, highlighting the importance of wide fields when studying the volume densities of massive sources like SMGs.

For a comparison against semianalytic model predictions we follow A. S. Long et al. (2023; see their Section 4.4) in extracting mock samples of actively star-forming galaxies with $\log M_*/M_\odot > 10.5$ and $\log L_{IR}/L_\odot > 11$ from SHARK (C. d. P. Lagos et al. 2019, 2020), which does a good job matching 850 μm number counts, and SIDES (M. Béthermin et al. 2017), which successfully reproduces the number counts of Herschel/PACS and SPIRE maps. The SCUBADive volume densities are in good agreement with SHARK at $z < 3$, but accounting for completeness in S2COSMOS could favor SIDES. At $z > 3$ the SCUBADive volume density is 0.3 $-$0.4 dex above SHARK and $\sim$0.5 dex below SIDES. A major conclusion of SHARK is that $S_{850} > 2$ mJy SMGs contribute negligibly to the volume-averaged star formation rate density at $z > 3$, which the SCUBADive measurements challenge by allowing for a $\sim$3$\times$ greater SMG volume density at $z > 3$ after accounting for incompleteness. This enhancement is exacerbated by the fact that an 850 μm selection on the highest-redshift, dusty star-forming galaxies might yield a subdominant population to those more efficiently selected at 2 mm (e.g., C. M. Casey et al. 2021; J. A. Zavala et al. 2021; O. R. Cooper et al. 2022; A. S. Long et al. 2024). Indeed, we compare against the ExMORA 2 mm blind survey over COSMOS from A. S. Long et al. (2024), which falls between the SHARK and SIDES models at $z > 5$. Combined with SCUBADive, the data do not rule out $S_{850} > 2$ mJy SMGs as potentially important contributors to the star formation rate density at $z > 3$ if they are confirmed to be $\sim$1 dex more numerous than the SHARK semianalytic model.

8.2. Selecting High-redshift Dusty Star-forming Galaxies with JWST Alone?

SCUBADive being a verified high-redshift, dusty star-forming galaxy sample matched to NIRCam and MIRI counterparts allows for tests on selection methods using JWST alone. These are of interest for subsets of high-z dusty galaxies that may harbor significant dust reservoirs but are not detected in wide-field SCUBA-2 submillimeter maps.

In SCUBADive there are 82 (28%) sources that satisfy the HST-dark selection criterion for massive, high-redshift, and obscured galaxies from L. Barrufet et al. (2023) and R. Gottumukkala et al. (2024): [F160W] $-$ [F444W] > 2.3. This subset of SCUBADive indeed consists of the highest-redshift members; however, it misses 44 (75%) $z > 3$ SCUBADive galaxies and 9 (32%) with $z > 4$.

Figure 11 shows a zoom-in to the F277W and F444W color–magnitude space also shown in Figure 4, but now highlighting the domain of $z > 3$ SMGs. We find that the following color and magnitude cuts in the F277W and F444W filters encase most of the high-z subset of SCUBADive with minimal contamination of lower-redshift SMGs:

$$\begin{aligned} &\text{(i)} && [\mathrm{F444W}] > 21 \\ &\text{(ii)} && [\mathrm{F277W}] - [\mathrm{F444W}] > 0.4 \\ &\text{(iii)} && [\mathrm{F277W}] - [\mathrm{F444W}] > \frac{[\mathrm{F444W}]}{5.25} - 3.98. \end{aligned}$$

We construct these color/magnitude cuts based on the limits of $z > 3$ SCUBADive sources and because 46 of the 63 $z > 3$ SMGs in SCUBADive have SNR < 5 in F115W and 29 have SNR < 5 in F150W. NIRCam/LW bands are best suited for selecting $z > 3$ SMGs, in part due to their faint fluxes below $\lambda_{obs} = 2\,\mu$m. The colors of $z > 3$ SCUBADive SMGs are consistent with $z = 3$–7 evolution in [F277W] $-$ [F444W] and [F444W] for template SEDs from ALESS at $A_V \geqslant 2$ (E. da Cunha et al. 2015). This selection may be useful for selecting $z > 3$ candidates, but ultimately spectroscopic follow-up is needed. Indeed, 70 SCUBADive galaxies with $z_{phot} < 3$ fall within the color/magnitude selection, but this is a strong function of the adopted lower [F444W] limit, falling to 18 low-z SMGs for [F444W] >22 and 2 with [F444W] > 23.

While the above selection wedge encases all but one of the $z > 3$ SMGs in SCUBADive, it does not exclusively capture this population. Galaxies of similar color can include LRDs, but these are point sources and can therefore be morphologically separated from SMGs (V. Kokorev et al. 2024). No SCUBADive galaxy is exclusively a point source in NIRCam, and none overlap with the sample of LRDs in COSMOS-Web from H. B. Akins et al. (2024). Many host point-source profiles in F444W, but always on top of other structure apparent in F444W and the shorter NIRCam bands. Recently different works using a selection function combining red JWST/NIRCam colors with a lack of detection in HST bands have uncovered a population of dust-obscured galaxies apparently below the SMG limit on dust masses but with nonnegligible dust obscuration (L. Barrufet et al. 2023; C. C. Williams et al. 2024). Based on spectroscopic follow-up of 24 objects, these sources have $z \sim 4$–5, $A_V > 2$ mag, and $\log M_*/M_\odot > 9.8$ (L. Barrufet et al. 2024). Given the masses and attenuation

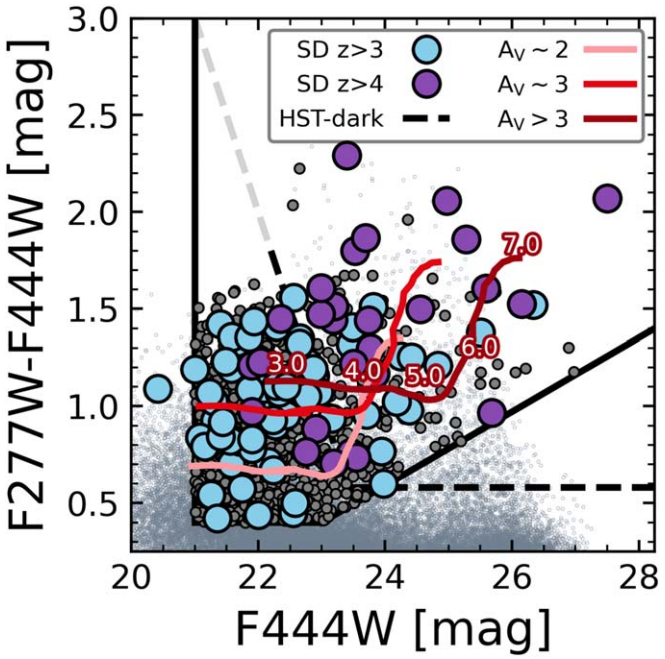

Figure 11. Zoom-in on the faint and red subset of COSMOS-Web sources in JWST/NIRCam's F277W and F444W color–magnitude space. In blue and purple we show SCUBADive sources at $z > 3$ and $z > 4$, respectively. The black solid line shows our color–magnitude wedge that encases $z > 3$ SCUBADive galaxies, some of which are missed by JWST-calibrated selections on massive galaxies that exclude sources brighter than F444W $\lesssim$ 23 mag (black dashed line; L. Barrufet et al. e.g., 2023; R. Gottumukkala et al. e.g., 2024). Gray circles within the solid black wedge represent 652 COSMOS-Web sources within the FWHM of a SCUBA-2 SMG from S2COSMOS (J. M. Simpson et al. 2019) and not already in SCUBADive, which, given the domain/range of both SCUBADive and $z = 3-7$ redshifted SED tracks for $A_V \sim 2$, 3 and $A_V > 3$ ALESS SMGs from E. da Cunha et al. (2015), are plausibly $z > 3$ dusty star-forming galaxies.

found among SCUBADive, these NIRCam-selected sources could be a less massive, less extreme tail of the $z > 3$ SMG population. Indeed, recent models suggest that $z = 4-5$ galaxies harbor $\sim 5\times$ more dust-obscured star formation than their $z = 0-2$ mass-matched counterparts (D. T. Zimmerman et al. 2024), which supports a heterogeneous population of $z > 3$ dust-obscured, star-forming galaxies, including the most extreme SMGs. Ultimately, differential dust geometry across an SMG can cause its optical/NIR colors to appear far less extreme (e.g., J. H. Howell et al. 2010; C. M. Casey et al. 2014b; R. K. Cochrane et al. 2024); hence, an overlap in colors with samples like those of L. Barrufet et al. (2023, 2024) and R. Gottumukkala et al. (2024) is unsurprising.

In addition to the aforementioned confusion with other galaxy populations, we should approach with caution NIRCam selection of SMG counterparts without high-resolution interferometer follow-up. There are some cases where red NIRCam colors can be a useful prior in predicting likely SMG counterparts (e.g., S. Gillman et al. 2023), but the technique is not guaranteed to select the true SMG. Discounting SMGs resolved into two or three ALMA sources, 50% of SCUBADive galaxies are not the reddest NIRCam source within the footprint of their SCUBA-2 detection, consistent with the findings of S. Gillman et al. (2024). Indeed, within our selection wedge in Figure 11 there are 652 NIRCam sources that are also within the FWHM of the SCUBA-2 beam and therefore plausible counterparts to the submillimeter emission. Of these, only 90 (14%) can be ruled out as SMGs given overlap with the available ALMA data. Applying the $z > 3$ fraction in SCUBADive to the whole sample, there should be 157 $z > 3$ SMGs in S2COSMOS + COSMOS-Web yet to have confirmed NIRCam counterparts. For these sources there are on average four candidate JWST counterparts that occupy the red and faint color space in Figure 11, highlighting the need for ALMA, NOEMA, SMA, and/or VLA follow-up to isolate the true optical counterparts to SMGs.

8.3. The Clustering of Sources around SMGs

Many works have proposed SMGs as signposts of overdense environments with respect to the large-scale structure of the Universe (D. L. Clements et al. 2014; H. Dannerbauer et al. 2014; C. M. Casey et al. 2015; D. L. Clements et al. 2016; I. Flores-Cacho et al. 2016; C.-L. Hung et al. 2016; T. Wang et al. 2016a; S. M. Stach et al. 2021; R. Calvi et al. 2023). However, there is outstanding controversy on this issue (e.g., S. C. Chapman et al. 2009; T. B. Miller et al. 2015; T. M. Cornish et al. 2024), and ultimately high-fidelity redshifts are needed to leverage SMGs and their companions to select (proto)cluster galaxy populations (T. B. Miller et al. 2015; C. C. Hayward et al. 2018; for a recent review, see S. Alberts & A. Noble 2022). Given the improvement on photometric redshifts with the added JWST data now available for COSMOS-Web (C. M. Casey et al. 2023b), we conduct a simple test on the overdensity around SCUBADive SMGs.

We construct a sample of candidate counterparts to SCUBADive galaxies, i.e., possible physical associations, by first searching COSMOS-Web for all NIRCam sources within 10″ of a SCUBADive coordinate. This corresponds to a physical search radius of approximately 100 kpc given the redshift range of SCUBADive, covering $\sim$30%–40% the virial radius of a $10^{13}\,M_\odot$ halo within which SCUBADive sources likely fall given their stellar masses (P. S. Behroozi et al. 2010). We then only consider the candidate companion galaxies with photometrically derived redshifts within 1σ of the SCUBADive source. While this is not the strictest method for removing objects with chance alignment, it does reflect allowable associations given the data at hand. In this manner we find 1870 candidate counterparts to SCUBADive galaxies corresponding to 7 ± 3 associations per source. For random points in the field with the same redshift distribution we expect as many as 10 ± 4 per source based on Monte Carlo simulations drawn from the catalog. Figure 12 shows the NIRCam SW (F115W − F150W) versus LW (F277W − F444W) color–color space occupied by both SCUBADive galaxies and their candidate companions, which exhibit colors inconsistent with the entirety of COSMOS-Web: candidate companions have, on average, redder colors in both the SW and LW bands by 0.15 and 0.3 dex, respectively, and the blue peak in F277W − F444W at -0.7 mag found for all of COSMOS-Web is not pronounced in the companion distribution. Figure 13 shows the two-point correlation function for the candidate companions, which we compute using `astroML` (J. VanderPlas et al. 2012; Ž. Ivezić et al. 2020).

To assess the statistical significance of clustering around SCUBADive sources, we create a series of test samples containing 289 sources/positions drawn from (a) the NIRCam color space occupied by SCUBADive, (b) the entire COSMOS-Web catalog, and (c) random positions in COSMOS-Web. For cases (a) and (b) we weight the draw of any particular source

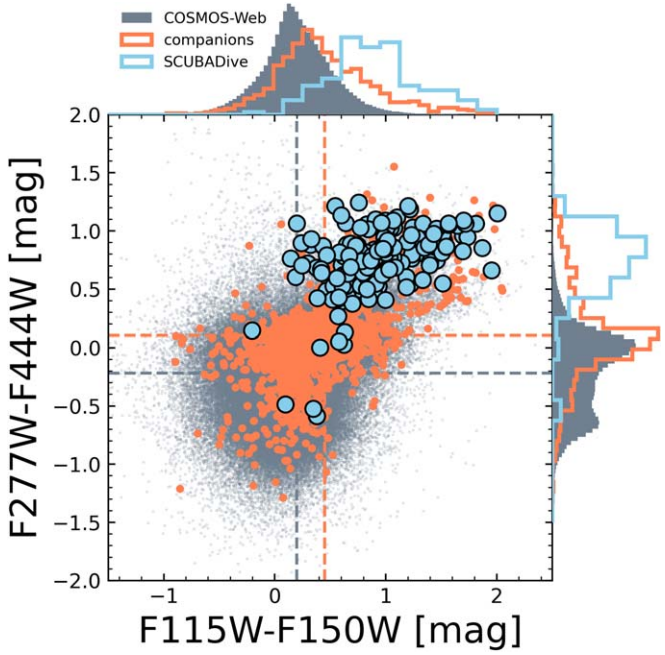

Figure 12. NIRCam SW and LW color–color space for SCUBADive detected in all four COSMOS-Web bands (blue), their candidate companions (orange), and the rest of the COSMOS-Web sources (gray). The respectively colored dashed lines correspond to the average colors of the COSMOS-Web and candidate companion data sets. The companions to SCUBADive galaxies exhibit redder NIRCam colors in both SW and LW bands than what would be expected from a randomly drawn sample from all COSMOS-Web sources.

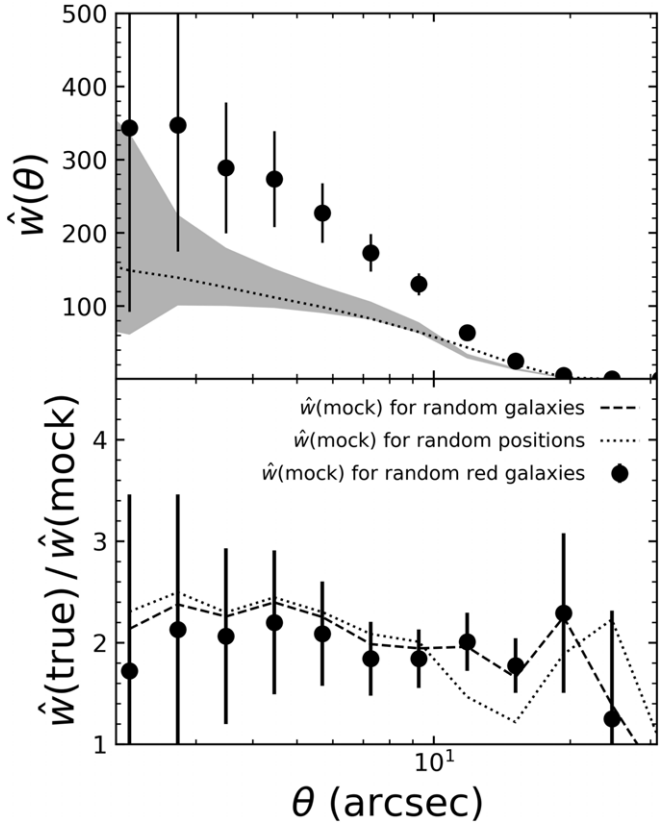

Figure 13. The clustering signal for sources around SCUBADive galaxies with consistent redshifts. Top: two-point angular correlation function $\hat{w}(\theta)$. With black circles we show $\hat{w}(\theta)$ for 1870 candidate companion galaxies within 10″ of a SCUBADive source and with a consistent photometric redshift within 1σ. The shaded gray region encases the bootstrapped range in $\hat{w}(\theta)$ derived for 1000 mock clustering catalogs generated semirandomly to match the NIRCam LW space of SCUBADive galaxies and their redshift distribution as described in Section 8.3. The black dotted line shows the two-point correlation function around random coordinates in COSMOS-Web, a baseline test against the significance of the SCUBADive clustering signal. Bottom: the ratio of our measured two-point angular correlation function to that of the average mock clustering catalogs for three different random selections as listed in the legend. Between ∼5″ and 20″ the clustering of our candidate companion sample is statistically significant at ∼2× what is expected based on the clustering around random galaxies and random positions in the field.

by the value of the normalized SCUBADive redshift distribution at its corresponding photometric redshift. This ensures a fair comparison against SCUBADive given redshift-dependent effects on the colors of galaxies. For each of these mock samples we then follow the previously described method for selecting candidate counterparts to build a mock candidate catalog, which we then use to calculate a two-point correlation function. We repeat this process 1000 times to bootstrap the two-point correlation function range. As shown in Figure 13, the two-point correlation function around SCUBADive sources is ∼2× that of all the mock catalogs between ∼5″ and 20″ and is statistically significant given the propagated uncertainties. In other words, the clustering strength around SMGs in SCUBADive is 2× that of the baseline for arbitrarily selected galaxies in COSMOS-Web, galaxies with similar colors to the SMGs in SCUBADive, and random positions in the field. We acknowledge that the significance of the two-point correlation function clustering signal around SMGs would most likely increase with better constraint on redshifts across the board and a more careful analysis of candidate companions; however, this analysis does corroborate the hypothesis that submillimeter-selected galaxies and, more generally, dusty star-forming galaxies reside within massive dark matter halos at the centers of overdense environments as discussed by many works in the literature (C. M. Casey 2016; J. Greenslade et al. 2018; T. Cheng et al. 2019; C. Gómez-Guijarro et al. 2019; S. Alberts & A. Noble 2022; R. Popescu et al. 2023). Future clustering work will investigate this in more detail.

9. Conclusions

In this work we present the SCUBADive project. We uncover the COSMOS-Web (C. M. Casey et al. 2023a) JWST/NIRCam counterparts to galaxies detected in the SCUBA-2 850 μm map of the COSMOS field (J. M. Simpson et al. 2019). Using every publicly available archival ALMA observation in Band 6 and 7 over COSMOS-Web, we resolve on subarcsecond scales the submillimeter emission from 219 SCUBA-2/850 μm sources into 289 galaxies. We then match these sources to the COSMOS-Web data, investigate their NIR morphologies, measure their NIRCam photometry, and fit the galaxy SEDs to derive redshifts and other physical properties. Our main conclusions are as follows:

1. We resolve 25% of 219 SCUBA-2 sources into multiple galaxies, 44 of which are doublets and nine of which are triplets. In some cases the member galaxies are obviously interacting with one another as evidenced by their NIRCam imaging.
2. The NIRCam/LW colors of SMGs are redder than 95% of all sources in COSMOS-Web. The highest-redshift SMGs in our catalog have [F277W] − [F444W] > 1.5 and [F444W] > 23, overlapping the color–magnitude space of other high-redshift, dusty galaxy populations

like LRDs and HST-dark galaxies. No SMG in SCUBADive is in the COSMOS-Web LRD sample of H. B. Akins et al. (2024).

3. Approximately 50% of the NIRCam counterparts to SMGs in SCUBADive do not have the reddest [F277W] − [F444W] color among nearby galaxies within the extent of the SCUBA-2 detection. Thus, NIRCam-alone selection methods may miss the true optical counterpart to an SMG ∼50% of the time, highlighting the need for interferometer follow-up to confirm counterpart association.
4. Fitting the optical-through-radio SEDs, we measure stellar masses of $\log M_*/M_\odot = 11.1^{+0.3}_{-0.5}$, fully consistent with other large samples of SMGs (e.g., U. Dudzevičiūtė et al. 2020). We find $\langle A_V \rangle = 2.5^{+1.5}_{-1.0}$ also in good agreement with past estimates of attenuation in SMGs; however, the faint subset of SCUBADive sources with [F444W] > 24 that also have $z > 3$ exhibit $\langle A_V \rangle = 4^{+1}_{-2}$, consistent with these sources having both higher redshifts and higher attenuation.
5. A total of 81 NIRCam sources have no prior optical/NIR counterpart in COSMOS2020. These represent the majority of $z > 4$ sources in SCUBADive and surprisingly a constant ∼25% fraction of SMGs between $1 < z < 4$. This "OIR-dark" subset has $\langle A_V \rangle = 3^{+2}_{-1.5}$ and $\log M_*/M_\odot = 11.1^{+0.4}_{-0.5}$.
6. The majority of SCUBADive sources either exhibit smooth Sérsic-like morphologies or are irregular/clumpy. We visually identify 50 candidate mergers, 32 SMGs with spiral arms, and 23 SMGs with candidate stellar bars. Most of the barred SMGs are at $z \sim 1-2$, but we also report a candidate stellar bar caught in the act of forming at $z = 3.4 \pm 1.3$. We observe dust emission in the cores of bar hosts and even nuclear NIRCam point sources, suggesting that stellar bars might positively affect the growth of a central stellar population, as well as the supermassive black hole.
7. We measure the volume density of SMGs in SCUBADive out to $z \sim 6$ and collapse the volume density uncertainty by a factor of 6 at $z > 4$ compared to prior works given (a) our source density at this epoch, (b) the reliability of our photometric redshifts, and most importantly (c) the large survey area of COSMOS-Web. Our volume densities fall between semianalytic models like SHARK (C. d. P. Lagos et al. 2019, 2020) and SIDES (M. Béthermin et al. 2017).
8. Based on a simple search for companion galaxies with similar redshifts to the SMGs in SCUBADive, we find the clustering of NIRCam-detected galaxies around SMGs to be greater than the clustering around randomly selected galaxies and random positions by a factor of 2. This is statistically significant but warrants future work to precisely measure the overdensity of companions around SMGs.

SCUBADive is an ongoing statistical project to study the JWST counterparts to SMGs. We have built a large sample of 289 galaxies complete with JWST and ALMA data, which are telling new stories about the in situ mass assembly of stars and supermassive black holes and the physical nature of SMGs. However, the sample remains incomplete. Within the COSMOS-Web area there are 706 SMGs, of which we have ALMA Band 6 and 7 detections for just 219 (≈31%). Assuming the multiplicity fraction in SCUBADive would imply ∼600 high-redshift, dusty star-forming galaxies yet to be unambiguously associated with their optical counterpart in existing JWST imaging. There are ongoing efforts with longer-wavelength ALMA imaging (ExMORA; A. S. Long et al. 2024) and radio counterpart matching with the VLA (M. Talia et al. 2025, in preparation; F. Gentile et al. 2025, in preparation) that may chip away at this unmatched population, but a dedicated follow-up program is needed to achieve a flux-limited SCUBADive data set. The outcome of such a program would be a multiwavelength census of SMGs out to $z \sim 6$ over the COSMOS field, including ∼30−50 more sources at $z > 4$ and ∼100 with $1 < z < 4$ that still elude detection by ground-based facilities and HST.

Acknowledgments

J.M. acknowledges the tremendous support of the NRAO Helpdesk Team in restoring calibrated data products from the ALMA archive and for making their remote computing resources readily accessible: many thanks to S. Wood, T. Ashton, and M. Sanchez in particular for facilitating access to the data. J.M. also acknowledges A. Pope for her guidance, K. Guo for her discussion on stellar bars, and I. Shivaei for providing MOSDEF catalogs. J.M. and A.S.L. acknowledge the invaluable labor of the maintenance and clerical staff at our institutions, whose contributions make our scientific discoveries a reality. J.M., A.S.L., S.M.M., and S.F. thank NASA and acknowledge support through the Hubble Fellowship Program, awarded by the Space Telescope Science Institute, which is operated by the Association of Universities for Research in Astronomy, Inc., for NASA, under contract NAS 5-26555. C. M.C. thanks the National Science Foundation for support through grants AST-2009577 and AST-2307006 and NASA for support through grant JWST-GO-0172.

Authors from UT Austin acknowledge that UT is an institution that sits on indigenous land. The Tonkawa lived in central Texas, and the Comanche and Apache moved through this area. We pay our respects to all the American Indian and Indigenous Peoples and communities who have been or have become a part of these lands and territories in Texas. We are grateful to be able to live, work, collaborate, and learn on this piece of Turtle Island.

The National Radio Astronomy Observatory is a facility of the National Science Foundation operated under cooperative agreement by Associated Universities, Inc. This paper makes use of the following ALMA data: ADS/JAO.ALMA#:2012.1.00978.S 2013.1.00034.S 2013.1.00118.S 2013.1.00151.S 2013.1.00208.S 2013.1.00815.S 2013.1.00884.S 2013.1.01292.S 2015.1.00055.S 2015.1.00137.S 2015.1.00260.S 2015.1.00379.S 2015.1.00568.S 2015.1.01074.S 2015.1.01345.S 2015.1.01495.S 2016.1.00279.S 2016.1.00463.S 2016.1.00478.S 2016.1.00646.S 2016.1.00735.S 2016.1.00804.S 2016.1.01184.S 2016.1.01208.S 2016.1.01604.S 2017.1.00046.S 2017.1.00326.S 2017.1.00428.L 2017.1.01276.S 2018.1.00635.S 2018.1.00874.S 2018.1.01044.S 2018.1.01281.S 2018.1.01871.S 2019.1.01142.S 2019.1.01275.S 2021.1.01133.S 2021.1.01328.S 2022.1.01493.S. ALMA is a partnership of ESO (representing its member states), NSF (USA) and NINS (Japan), together with NRC (Canada), MOST and ASIAA (Taiwan), and KASI (Republic of Korea), in cooperation with the Republic of Chile. The Joint ALMA Observatory is operated by ESO, AUI/NRAO and NAOJ.

This work is based (in part) on observations made with the NASA/ESA/CSA James Webb Space Telescope. The data were obtained from the Mikulski Archive for Space Telescopes at the Space Telescope Science Institute, which is operated by the Association of Universities for Research in Astronomy, Inc., under NASA contract NAS 5-03127 for JWST. These observations are associated with program nos. 1727 and 1837. This work was funded (in part) by support for program no. 1727 provided by NASA through a grant from the Space Telescope Science Institute, which is operated by the Association of Universities for Research in Astronomy, Inc., under NASA contract NAS 5-03127.

Appendix

This appendix shows example JWST/NIRCam RGBs for a subset of SCUBADive (Figure 14). The complete figure set (290 images) is available in the online journal.

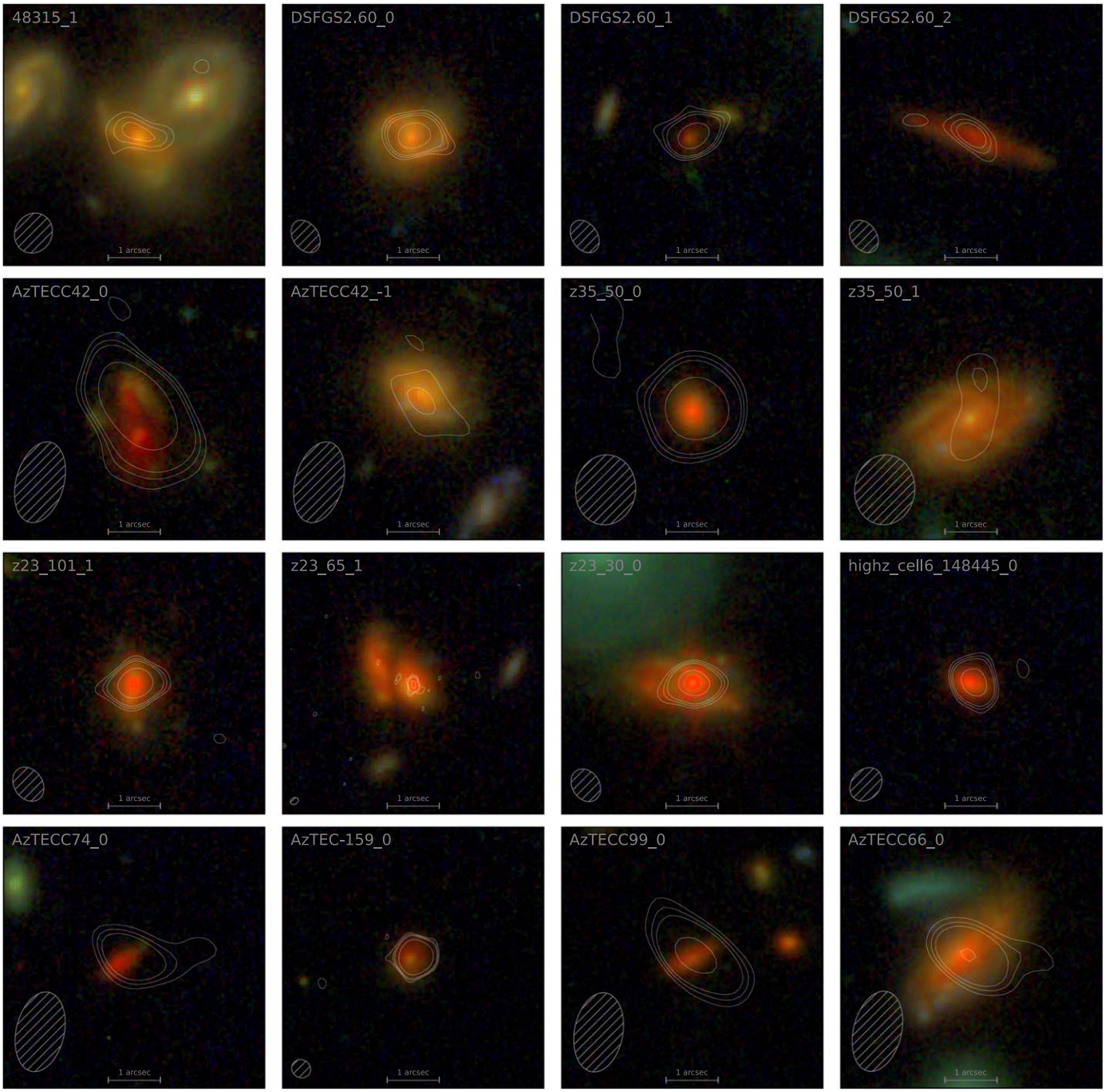

Figure 14. JWST/NIRCam RGBs (B = F115W+F150W, G = F277W, R = F444W) of SCUBADive galaxies using data from the COSMOS-Web program. ALMA contours are drawn in white at 3σ, 4σ, 5σ, and 10σ, with the ALMA beam shown in the lower left corner. Each image is $5'' \times 5''$. The complete figure set (290 images) is available in the online journal.

(The complete figure set (290 images) is available in the online article.)

ORCID iDs

Jed McKinney https://orcid.org/0000-0002-6149-8178
Caitlin M. Casey https://orcid.org/0000-0002-0930-6466
Arianna S. Long https://orcid.org/0000-0002-7530-8857
Olivia R. Cooper https://orcid.org/0000-0003-3881-1397
Sinclaire M. Manning https://orcid.org/0000-0003-0415-0121
Maximilien Franco https://orcid.org/0000-0002-3560-8599
Hollis Akins https://orcid.org/0000-0003-3596-8794
Erini Lambrides https://orcid.org/0000-0003-3216-7190
Elaine Gammon https://orcid.org/0009-0007-0553-9610
Camila Silva https://orcid.org/0000-0002-0113-7784
Fabrizio Gentile https://orcid.org/0000-0002-8008-9871
Jorge A. Zavala https://orcid.org/0000-0002-7051-1100
Aristeidis Amvrosiadis https://orcid.org/0000-0002-4465-1564
Irham Andika https://orcid.org/0000-0001-6102-9526
Malte Brinch https://orcid.org/0000-0002-0245-6365
Jaclyn B. Champagne https://orcid.org/0000-0002-6184-9097
Nima Chartab https://orcid.org/0000-0003-3691-937X
Nicole E. Drakos https://orcid.org/0000-0003-4761-2197
Andreas L. Faisst https://orcid.org/0000-0002-9382-9832
Seiji Fujimoto https://orcid.org/0000-0001-7201-5066
Steven Gillman https://orcid.org/0000-0001-9885-4589
Ghassem Gozaliasl https://orcid.org/0000-0002-0236-919X
Thomas R. Greve https://orcid.org/0000-0002-2554-1837
Santosh Harish https://orcid.org/0000-0003-0129-2079
Christopher C. Hayward https://orcid.org/0000-0003-4073-3236
Michaela Hirschmann https://orcid.org/0000-0002-3301-3321
Olivier Ilbert https://orcid.org/0000-0002-7303-4397
Boris S. Kalita https://orcid.org/0000-0001-9215-7053
Jeyhan S. Kartaltepe https://orcid.org/0000-0001-9187-3605
Anton M. Koekemoer https://orcid.org/0000-0002-6610-2048
Vasily Kokorev https://orcid.org/0000-0002-5588-9156
Daizhong Liu https://orcid.org/0000-0001-9773-7479
Georgios Magdis https://orcid.org/0000-0002-4872-2294
Henry Joy McCracken https://orcid.org/0000-0002-9489-7765
Jason Rhodes https://orcid.org/0000-0002-4485-8549
Brant E. Robertson https://orcid.org/0000-0002-4271-0364
Margherita Talia https://orcid.org/0000-0003-4352-2063
Francesco Valentino https://orcid.org/0000-0001-6477-4011
Aswin P. Vijayan https://orcid.org/0000-0002-1905-4194

References

Akins, H. B., Casey, C. M., Lambrides, E., et al. 2024, arXiv:2406.10341
Alberts, S., & Noble, A. 2022, Univ, 8, 554
Algera, H. S. B., Inami, H., Sommovigo, L., et al. 2024, MNRAS, 527, 6867
Álvarez Crespo, N., Smolić, V., Finoguenov, A., Barrufet, L., & Aravena, M. 2021, A&A, 646, A174
An, F. X., Stach, S. M., Smail, I., et al. 2018, ApJ, 862, 101
Aretxaga, I., Wilson, G. W., Aguilar, E., et al. 2011, MNRAS, 415, 3831
Barger, A. J., Cowie, L. L., & Richards, E. A. 2000, AJ, 119, 2092
Barger, A. J., Cowie, L. L., Sanders, D. B., et al. 1998, Natur, 394, 248
Barger, A. J., Cowie, L. L., & Wang, W. H. 2007, ApJ, 654, 764
Barrufet, L., Oesch, P., Marques-Chaves, R., et al. 2024, arXiv:2404.08052
Barrufet, L., Oesch, P. A., Weibel, A., et al. 2023, MNRAS, 522, 449
Battisti, A. J., da Cunha, E., Grasha, K., et al. 2019, ApJ, 882, 61
Behroozi, P. S., Conroy, C., & Wechsler, R. H. 2010, ApJ, 717, 379
Bertin, E., & Arnouts, S. 1996, A&AS, 117, 393
Béthermin, M., Wu, H.-Y., Lagache, G., et al. 2017, A&A, 607, A89
Boquien, M., Burgarella, D., Roehlly, Y., et al. 2019, A&A, 622, A103
Borys, C., Smail, I., Chapman, S. C., et al. 2005, ApJ, 635, 853
Boucaud, A., Bocchio, M., Abergel, A., et al. 2016, A&A, 596, A63
Bradley, L., Sipőcz, B., Robitaille, T., et al. 2023, astropy/photutils: v1.8.0, Zenodo, doi: 10.5281/zenodo.7946442
Brinch, M., Greve, T. R., Sanders, D. B., et al. 2024, MNRAS, 527, 6591
Brisbin, D., Miettinen, O., Aravena, M., et al. 2017, A&A, 608, A15
Calvi, R., Castignani, G., & Dannerbauer, H. 2023, A&A, 678, A15
Capak, P., Aussel, H., Ajiki, M., et al. 2007, ApJS, 172, 99
Carnall, A. C., Leja, J., Johnson, B. D., et al. 2019, ApJ, 873, 44
Casey, C. M. 2016, ApJ, 824, 36
Casey, C. M., Chapman, S. C., Beswick, R. J., et al. 2009, MNRAS, 399, 121
Casey, C. M., Chen, C.-C., Cowie, L. L., et al. 2013, MNRAS, 436, 1919
Casey, C. M., Cooray, A., Capak, P., et al. 2015, ApJL, 808, L33
Casey, C. M., Kartaltepe, J. S., Drakos, N. E., et al. 2023a, ApJ, 954, 31
Casey, C. M., Kartaltepe, J. S., Drakos, N. E., et al. 2023b, arXiv:2211.07865
Casey, C. M., Narayanan, D., & Cooray, A. 2014a, PhR, 541, 45
Casey, C. M., Scoville, N. Z., Sanders, D. B., et al. 2014b, ApJ, 796, 95
Casey, C. M., Zavala, J. A., Aravena, M., et al. 2019, ApJ, 887, 55
Casey, C. M., Zavala, J. A., Manning, S. M., et al. 2021, ApJ, 923, 215
Casey, C. M., Zavala, J. A., Spilker, J., et al. 2018, ApJ, 862, 77
Chabrier, G. 2003, PASP, 115, 763
Chapman, S. C., Blain, A., Ibata, R., et al. 2009, ApJ, 691, 560
Chapman, S. C., Blain, A. W., Ivison, R. J., & Smail, I. R. 2003, Natur, 422, 695
Chapman, S. C., Blain, A. W., Smail, I., & Ivison, R. J. 2005, ApJ, 622, 772
Chapman, S. C., Smail, I., Windhorst, R., Muxlow, T., & Ivison, R. J. 2004, ApJ, 611, 732
Charlot, S., & Fall, S. M. 2000, ApJ, 539, 718
Chen, C.-C., Cowie, L. L., Barger, A. J., et al. 2013, ApJ, 776, 131
Chen, C.-C., Gao, Z.-K., Hsu, Q.-N., et al. 2022a, ApJL, 939, L7
Chen, C.-C., Liao, C.-L., Smail, I., et al. 2022b, ApJ, 929, 159
Chen, Z., Fang, G., Lin, Z., et al. 2021, ApJ, 906, 71
Cheng, C., Yan, H., Huang, J.-S., et al. 2022, ApJL, 936, L19
Cheng, T., Clements, D. L., Greenslade, J., et al. 2019, MNRAS, 490, 3840
Civano, F., Marchesi, S., Comastri, A., et al. 2016, ApJ, 819, 62
Clements, D. L., Braglia, F., Petitpas, G., et al. 2016, MNRAS, 461, 1719
Clements, D. L., Braglia, F. G., Hyde, A. K., et al. 2014, MNRAS, 439, 1193
Cochrane, R. K., Anglés-Alcázar, D., Cullen, F., & Hayward, C. C. 2024, ApJ, 961, 37
Cooper, O. R., Casey, C. M., Zavala, J. A., et al. 2022, ApJ, 930, 32
Cornish, T. M., Wardlow, J., Wade, H., et al. 2024, arXiv:2408.00063
Cowie, L. L., González-López, J., Barger, A. J., et al. 2018, ApJ, 865, 106
da Cunha, E., Charlot, S., & Elbaz, D. 2008, MNRAS, 388, 1595
da Cunha, E., Hodge, J. A., Casey, C. M., et al. 2021, ApJ, 919, 30
da Cunha, E., Walter, F., Smail, I. R., et al. 2015, ApJ, 806, 110
Damjanov, I., Zahid, H. J., Geller, M. J., Fabricant, D. G., & Hwang, H. S. 2018, ApJS, 234, 21
Dannerbauer, H., Kurk, J. D., De Breuck, C., et al. 2014, A&A, 570, A55
Delvecchio, I., Daddi, E., Sargent, M. T., et al. 2021, A&A, 647, A123
Draine, B. T., Aniano, G., Krause, O., et al. 2014, ApJ, 780, 172
Draine, B. T., & Li, A. 2007, ApJ, 657, 810
Drew, P. M., & Casey, C. M. 2022, ApJ, 930, 142
Dudzevičiūtė, U., Smail, I., Swinbank, A. M., et al. 2020, MNRAS, 494, 3828
Dunlop, J. S., Abraham, R. G., Ashby, M. L. N., et al. 2021, PRIMER: Public Release IMaging for Extragalactic Research, JWST Proposal. Cycle 1, ID. #1837
Eales, S., Lilly, S., Gear, W., et al. 1999, ApJ, 515, 518
Epinat, B., Contini, T., Mercier, W., et al. 2024, A&A, 683, A205
Euclid Collaboration, Moneti, A., McCracken, H. J., et al. 2022, A&A, 658, A126
Flores-Cacho, I., Pierini, D., Soucail, G., et al. 2016, A&A, 585, A54
Franco, M., Elbaz, D., Béthermin, M., et al. 2018, A&A, 620, A152
Fujimoto, S., Bezanson, R., Labbe, I., et al. 2023, arXiv:2309.07834
Gall, C., Andersen, A. C., & Hjorth, J. 2011, A&A, 528, A13
Geach, J. E., Dunlop, J. S., Halpern, M., et al. 2017, MNRAS, 465, 1789
Gentile, F., Talia, M., Behiri, M., et al. 2024, ApJ, 962, 26
Gillman, S., Gullberg, B., Brammer, G., et al. 2023, A&A, 676, A26
Gillman, S., Smail, I., Gullberg, B., et al. 2024, arXiv:2406.03544
Gómez-Guijarro, C., Riechers, D. A., Pavesi, R., et al. 2019, ApJ, 872, 117
Gottumukkala, R., Barrufet, L., Oesch, P. A., et al. 2024, MNRAS, 530, 966
Greenslade, J., Clements, D. L., Cheng, T., et al. 2018, MNRAS, 476, 3336

Gullberg, B., Smail, I., Swinbank, A. M., et al. 2019, MNRAS, 490, 4956
Guo, Y., Jogee, S., Finkelstein, S. L., et al. 2023, ApJL, 945, L10
Hainline, L. J., Blain, A. W., Smail, I., et al. 2009, ApJ, 699, 1610
Hainline, L. J., Blain, A. W., Smail, I., et al. 2011, ApJ, 740, 96
Hasinger, G., Capak, P., Salvato, M., et al. 2018, ApJ, 858, 77
Hayward, C. C., Chapman, S. C., Steidel, C. C., et al. 2018, MNRAS, 476, 2278
Hezaveh, Y. D., Marrone, D. P., Fassnacht, C. D., et al. 2013, ApJ, 767, 132
Hodge, J. A., & da Cunha, E. 2020, RSOS, 7, 200556
Hodge, J. A., da Cunha, E., Kendrew, S., et al. 2024, arXiv:2407.15846
Hodge, J. A., Karim, A., Smail, I., et al. 2013, ApJ, 768, 91
Hodge, J. A., Swinbank, A. M., Simpson, J. M., et al. 2016, ApJ, 833, 103
Hopkins, P. F., Hernquist, L., Cox, T. J., & Kereš, D. 2008, ApJS, 175, 356
Horowitz, B., Lee, K.-G., Ata, M., et al. 2022, ApJS, 263, 27
Howell, J. H., Armus, L., Mazzarella, J. M., et al. 2010, ApJ, 715, 572
Hughes, D. H., Serjeant, S., Dunlop, J., et al. 1998, Natur, 394, 241
Hung, C.-L., Casey, C. M., Chiang, Y.-K., et al. 2016, ApJ, 826, 130
Hurley, P. D., Oliver, S., Betancourt, M., et al. 2017, MNRAS, 464, 885
Ivezić, Ž., Connolly, A. J., VanderPlas, J. T., & Gray, A. 2020, Statistics, Data Mining, and Machine Learning in Astronomy: A Practical Python Guide for the Analysis of Survey Data, Updated Edition (New York: de Gruyter & Co),
Jiménez-Andrade, E. F., Zavala, J. A., Magnelli, B., et al. 2020, ApJ, 890, 171
Jin, S., Daddi, E., Magdis, G. E., et al. 2019, ApJ, 887, 144
Jin, S., Sillassen, N. B., Hodge, J., et al. 2024, A&A, 690, L16
Jogee, S., Barazza, F. D., Rix, H.-W., et al. 2004, ApJL, 615, L105
Karim, A., Swinbank, A. M., Hodge, J. A., et al. 2013, MNRAS, 432, 2
Kartaltepe, J. S., Sanders, D. B., Silverman, J. D., et al. 2015, ApJL, 806, L35
Kashino, D., Silverman, J. D., Sanders, D., et al. 2019, ApJS, 241, 10
Kirkpatrick, A., Pope, A., Sajina, A., et al. 2015, ApJ, 814, 9
Koekemoer, A. M., Aussel, H., Calzetti, D., et al. 2007, ApJS, 172, 196
Kokorev, V., Caputi, K. I., Greene, J. E., et al. 2024, arXiv:2401.09981
Kokorev, V., Jin, S., Magdis, G. E., et al. 2023, ApJL, 945, L25
Kriek, M., Shapley, A. E., Reddy, N. A., et al. 2015, ApJS, 218, 15
Krogager, J. K., Zirm, A. W., Toft, S., Man, A., & Brammer, G. 2014, ApJ, 797, 17
Lagos, C. d. P., da Cunha, E., Robotham, A. S. G., et al. 2020, MNRAS, 499, 1948
Lagos, C. d. P., Robotham, A. S. G., Trayford, J. W., et al. 2019, MNRAS, 489, 4196
Le Bail, A., Daddi, E., Elbaz, D., et al. 2024, A&A, 688, A53
Le Floc'h, E., Aussel, H., Ilbert, O., et al. 2009, ApJ, 703, 222
Liang, L., Feldmann, R., Kereš, D., et al. 2019, MNRAS, 489, 1397
Lilly, S. J., Le Fèvre, O., Renzini, A., et al. 2007, ApJS, 172, 70
Long, A. S., Casey, C. M., del P. Lagos, C., et al. 2023, ApJ, 953, 11
Long, A. S., Casey, C. M., McKinney, J., et al. 2024, arXiv:2408.14546
Lutz, D., Poglitsch, A., Altieri, B., et al. 2011, A&A, 532, A90
Madau, P., & Dickinson, M. 2014, ARA&A, 52, 415
Manning, S. M., Casey, C. M., Zavala, J. A., et al. 2022, ApJ, 925, 23
Marchesi, S., Civano, F., Elvis, M., et al. 2016, ApJ, 817, 34
Marinova, I., & Jogee, S. 2007, ApJ, 659, 1176
McKinney, J., Finnerty, L., Casey, C. M., et al. 2023a, ApJL, 946, L39
McKinney, J., Hayward, C. C., Rosenthal, L. J., et al. 2021, ApJ, 921, 55
McKinney, J., Manning, S. M., Cooper, O. R., et al. 2023b, ApJ, 956, 72
McMullin, J. P., Waters, B., Schiebel, D., Young, W., & Golap, K. 2007, in ASP Conf. Ser. 376, Astronomical Data Analysis Software and Systems XVI, ed. R. A. Shaw, F. Hill, & D. J. Bell (San Francisco, CA: ASP), 127
Michałowski, M. J., Dunlop, J. S., Cirasuolo, M., et al. 2012, A&A, 541, A85
Michałowski, M. J., Hayward, C. C., Dunlop, J. S., et al. 2014, A&A, 571, A75
Miettinen, O., Delvecchio, I., Smolåić, V., et al. 2017, A&A, 606, A17
Miller, T. B., Hayward, C. C., Chapman, S. C., & Behroozi, P. S. 2015, MNRAS, 452, 878
Mitsuhashi, I., Matsuda, Y., Smail, I., et al. 2021, ApJ, 907, 122
Mohan, N., & Rafferty, D., 2015 PyBDSF: Python Blob Detection and Source Finder, Astrophysics Source Code Library, ascl:1502.007
Moster, B. P., Somerville, R. S., Newman, J. A., & Rix, H.-W. 2011, ApJ, 731, 113
Murphy, E. J., Chary, R. R., Dickinson, M., et al. 2011, ApJ, 732, 126
Nanayakkara, T., Glazebrook, K., Kacprzak, G. G., et al. 2016, ApJ, 828, 21
Oke, J. B. 1974, ApJS, 27, 21
Oliver, S. J., Bock, J., Altieri, B., et al. 2012, MNRAS, 424, 1614
Onodera, M., Carollo, C. M., Renzini, A., et al. 2015, ApJ, 808, 161
Pearson, J., Serjeant, S., Wang, W.-H., et al. 2024, MNRAS, 527, 12044
Popescu, R., Pope, A., Lee, K.-S., et al. 2023, ApJ, 958, 12
Popping, G., Somerville, R. S., & Galametz, M. 2017, MNRAS, 471, 3152
Price, S. H., Suess, K. A., Williams, C. C., et al. 2023, arXiv:2310.02500
Reddy, N. A., Kriek, M., Shapley, A. E., et al. 2015, ApJ, 806, 259
Rujopakarn, W., Williams, C. C., Daddi, E., et al. 2023, ApJL, 948, L8
Sanders, D. B., & Mirabel, I. F. 1996, ARA&A, 34, 749
Sanders, D. B., Salvato, M., Aussel, H., et al. 2007, ApJS, 172, 86
Schinnerer, E., Sargent, M. T., Bondi, M., et al. 2010, ApJS, 188, 384
Schreiber, C., Elbaz, D., Pannella, M., et al. 2018, A&A, 609, A30
Scoville, N., Aussel, H., Brusa, M., et al. 2007, ApJS, 172, 1
Shah, E. A., Kartaltepe, J. S., Magagnoli, C. T., et al. 2020, ApJ, 904, 107
Shivaei, I., Reddy, N. A., Shapley, A. E., et al. 2015, ApJ, 815, 98
Simpson, J. M., Smail, I., Dudzevičiūtė, U., et al. 2020, MNRAS, 495, 3409
Simpson, J. M., Smail, I., Swinbank, A. M., et al. 2019, ApJ, 880, 43
Simpson, J. M., Swinbank, A. M., Smail, I., et al. 2014, ApJ, 788, 125
Smail, I., Dudzevičiūtė, U., Gurwell, M., et al. 2023, ApJ, 958, 36
Smail, I., Dudzevičiūtė, U., Stach, S. M., et al. 2021, MNRAS, 502, 3426
Smail, I., Ivison, R. J., & Blain, A. W. 1997, ApJL, 490, L5
Smolčić, V., Miettinen, O., Tomiåić, O., et al. 2017a, A&A, 597, A4
Smolčić, V., Novak, M., Bondi, M., et al. 2017b, A&A, 602, A1
Solimano, M., González-López, J., Aravena, M., et al. 2024, A&A, 689, A145
Sommovigo, L., Ferrara, A., Pallottini, A., et al. 2022, MNRAS, 513, 3122
Stach, S. M., Smail, I., Amvrosiadis, A., et al. 2021, MNRAS, 504, 172
Storey-Fisher, K., Hogg, D. W., Rix, H.-W., et al. 2024, ApJ, 964, 69
Stott, J. P., Swinbank, A. M., Johnson, H. L., et al. 2016, MNRAS, 457, 1888
Swinbank, A. M., Smail, I., Chapman, S. C., et al. 2004, ApJ, 617, 64
Swinbank, A. M., Smail, I., Chapman, S. C., et al. 2010, MNRAS, 405, 234
Talia, M., Cimatti, A., Giulietti, M., et al. 2021, ApJ, 909, 23
Toft, S., Smolčić, V., Magnelli, B., et al. 2014, ApJ, 782, 68
Trenti, M., & Stiavelli, M. 2008, ApJ, 676, 767
Uematsu, R., Ueda, Y., Kohno, K., et al. 2024, ApJ, 965, 108
Valentino, F., Tanaka, M., Davidzon, I., et al. 2020, ApJ, 889, 93
VanderPlas, J., Connolly, A. J., Ivezic, Z., & Gray, A. 2012, Proc. Conf. Intelligent Data Understanding (CIDU), 2012, 47
Viero, M. P., Sun, G., Chung, D. T., Moncelsi, L., & Condon, S. S. 2022, MNRAS, 516, L30
Walter, F., Decarli, R., Carilli, C., et al. 2012, Natur, 486, 233
Wang, S. X., Brandt, W. N., Luo, B., et al. 2013, ApJ, 778, 179
Wang, T., Elbaz, D., Daddi, E., et al. 2016a, ApJ, 828, 56
Wang, T., Elbaz, D., Schreiber, C., et al. 2016b, ApJ, 816, 84
Wardlow, J. L., Smail, I., Coppin, K. E. K., et al. 2011, MNRAS, 415, 1479
Weaver, J. R., Kauffmann, O. B., Ilbert, O., et al. 2022, ApJS, 258, 11
Weiß, A., Ivison, R. J., Downes, D., et al. 2009, ApJL, 705, L45
Williams, C. C., Alberts, S., Ji, Z., et al. 2024, ApJ, 968, 34
Williams, C. C., Labbe, I., Spilker, J., et al. 2019, ApJ, 884, 154
Wu, Y., Cai, Z., Sun, F., et al. 2023, ApJL, 942, L1
Zavala, J. A., Buat, V., Casey, C. M., et al. 2023, ApJL, 943, L9
Zavala, J. A., Casey, C. M., Manning, S. M., et al. 2021, ApJ, 909, 165
Zimmerman, D. T., Narayanan, D., Whitaker, K. E., & Davè, R. 2024, ApJ, 973, 146